Organic Complexation of Iron by Strong Ligands and Siderophores in the Eastern Tropical North Pacific Oxygen Deficient Zone

[1,*]Laura E. Moore, [2, 3]Maija I. Heller, [4]Katherine A. Barbeau, [5]James W. Moffett, [1]Randelle M. Bundy

[1]School of Oceanography, University of Washington, Seattle, WA, USA
[2]Pontifica Universidad Católica de Valparaíso Chile, Valparaíso, Chile
[2]Escuela de Ciencias del Mar, Facultad de Ciencias del Mar y Geografiá , Pontifica Universidad Catoĺica de Valparaíso, Valparaíso, Chile; [3]Instituto Milenio de Oceanografía, Chile

[4]Geosciences Research Division, Scripps Institution of Oceanography, University of California, San Diego, La Jolla, CA, USA
[5]Department of Biological Sciences, University of Southern California, Los Angeles, CA, USA

[*]Corresponding author: Laura E. Moore, moore23@uw.edu

Keywords: Iron; Ligands; Chemical Speciation; Voltammetry; Siderophores; Oxygen Deficient Zone; Eastern Tropical North Pacific

Abstract

Continental margins are an important external source of dissolved iron to the marine environment. However, the mechanisms responsible for the offshore transport of dissolved iron is impacted by the resulting iron speciation. We characterized the iron speciation in the Eastern Tropical North Pacific (ETNP) oxygen deficient zone (ODZ), including dissolved iron, organic iron-binding ligands, and reduced iron. Organic iron-binding ligands were measured using both competitive ligand exchange adsorptive cathodic stripping voltammetry (CLE-ACSV) and liquid chromatography electrospray ionization mass spectrometry (LC-ESI-MS) in order to explore the impact of organic ligands on dissolved iron and iron(II) biogeochemistry in the region. Organic ligands were present in high concentrations (1.06-5.30 nmol L^{-1}) and exceeded dissolved iron concentrations (0.36-4.52 nmol L^{-1}) at all locations. Iron-binding strengths (log $K^{cond}_{FeL,Fe'}$) ranged 11.22 to 12.75 and were elevated in the ODZ layer relative to the oxygenated water column. LC-ESI-MS revealed the presence of siderophores, or bacterially-produced organic ligands with high Fe-affinity, in all samples analyzed, suggesting these compounds may be produced by microbes in the ODZ despite high ambient dFe_T concentrations. This study is the first to characterize siderophores in an ODZ environment to date, and the three siderophores found (amphibactin B, synechobactin c9, synechobactin c10) could contribute to the observed elevated log $K^{cond}_{FeL,Fe'}$ of ligands in the ODZ. Comparative analysis of organic ligand log $K^{cond}_{FeL,Fe'}$ ~~logK~~ values in other low oxygen environments suggests that strong ligands, including siderophores, could be present in other low oxygen regions. In a simple model of the shelf-to-offshore iron transport mechanism, strong organic iron-binding ligands had a large impact on the longevity and transport of iron in the ODZ. These results suggest that organic ligand composition can have an impact on iron distributions in the ETNP ODZ and regulate the offshore transport of iron to the open ocean.

1. Introduction

Iron (Fe) is an essential life-supporting element across the global ocean. As an important cofactor in cellular processes ranging from photosynthesis to nitrogen fixation, Fe exerts control on CO_2 uptake, macronutrient availability, and primary production (Morel and Price, 2003). Although one of the most abundant elements on earth, Fe is a limiting nutrient in an estimated 30-40% of the ocean and rarely exceeds 1 nmol L^{-1} in concentration (Moore et al., 2013). Characterizing Fe biogeochemistry is therefore crucial for understanding and predicting biomass distributions and climate impacts. Despite large advances in scientific understanding of the Fe cycle (Tagliabue et al., 2017), the key sources and sinks of Fe are still not well understood. For example, a comparison across thirteen global biogeochemical models that include Fe biochemistry show almost a two order of magnitude range in the total Fe inputs in the models (Tagliabue et al., 2016). The thirteen models also have dissolved Fe residence times ranging from 5 to greater than 500 years, and three of the models do not contain any sediment Fe sources despite the documented impact of margins on Fe biogeochemistry (Johnson et al., 1999; Lam et al., 2006; Lam and Bishop, 2008).

Models that do include sediment sources estimate that sediments are the most important Fe source in approximately 74% of the ocean by area (Tagliabue et al., 2014). This sedimentary Fe can be upwelled at eastern boundary margins and help to drive the high productivity commonly associated with coastal regions (Johnson et al., 1999). However, the effects of the sedimentary Fe flux extend far beyond local impacts. Sediment-sourced Fe has been tracked as far as 1,000 km from the nearest margin, and this Fe contributes to phytoplankton blooms in the North Pacific HNLC region (Lam et al., 2006; Lam and Bishop, 2008), highlighting the downstream biological impacts of this important Fe source. Relatively higher concentrations of Fe have been found in the pore waters of sediment cores underlying oxygen minimum zones (OMZs; < 90 μM O_2), corresponding with higher observed benthic Fe fluxes and elevated concentrations of reduced Fe (Fe(II)) (Elrod et al., 2004; Lohan and Bruland, 2008). Margins with low bottom water oxygen content, but are not yet sulfidic, have been shown to have the most efficient export of Fe from the margin (Scholz et al., 2014). These studies suggest that continental margins associated with OMZs, and by extension oxygen deficient zones (ODZs; < 2 μM O_2), might play a disproportionally large role in Fe supply to the ocean and may further enhance the export of Fe from margin sediments to the open ocean.

The Eastern Tropical North Pacific (ETNP) near the southwestern Mexican coast, is one potentially important coastal margin. Here, highly productive surface waters resulting from strong coastal upwelling drive the formation of the world's largest permanent ODZ (Horak et al., 2016). Organic matter degradation combined with low water column ventilation result in layers of suboxic (< 20 μM O_2) and anoxic (< 2 μM O_2) waters (Fiedler and Talley, 2006). Under these conditions, Fe can exist in both its oxidized (Fe(III)) and reduced (Fe(II)) states (e.g. Moffett et al., 2007), unlike the oxygenated ocean in which Fe is almost exclusively Fe(III) (Millero et al., 1995). The presence of Fe(II) introduces additional reaction pathways for both biotic and abiotic processes and likely plays an important role in Fe biogeochemistry in the ODZ. For instance, anaerobic Fe-oxidizing bacteria have been proposed as an important mediator of Fe oxidation reactions in ODZs (Croot et al., 2019). On a global scale, ODZs in particular may facilitate the transport of Fe from the continental shelf to the open ocean (Scholtz et al., 2014). In shelf

systems with an oxygenated water column, soluble Fe(II) is released from reducing sediments into the water column, and is then rapidly oxidized to insoluble Fe(III), effectively "trapping" Fe on the shelf (Vedamati et al., 2014). In an ODZ, low O_2 increases the longevity of Fe(II) released from the margin (Kondo and Moffett, 2013), possibly providing a mechanism by which Fe can escape the shelf. Observations along the Peru margin in the ODZ suggest that the long-range transport of Fe off the shelf is not in the core of the ODZ, but below the Fe(II) max on the shelf slope (Lam et. al 2020). Therefore, the mechanism for transport of total dissolved Fe (dFe_T) off the shelf in low oxygen systems remains unclear. It appears that inorganic and redox properties of Fe alone, are insufficient to describe the complicated dynamics of off shelf transport of dFe_T in these systems.

Although Fe redox reactions in the ODZ are suspected to be the primary driver for Fe transformations in the ODZ, an estimated > 99% of the dFe_T in the ocean is bound to organic ligands (Rue and Bruland, 1995), an observation that has been supported in ODZ environments as well (Glass et al., 2015; Hopkinson and Barbeau, 2007; Kondo and Moffett, 2015; Witter et al., 2000). These organic Fe-binding ligands increase the solubility of Fe(III) in seawater and help govern the bioavailability, reactivity and transport of dFe_T (Buck et al., 2018; Gledhill and Buck, 2012; Hunter and Boyd, 2007; Rose and Waite, 2003). Previous studies in the ETNP, Eastern Tropical South Pacific (ETSP), and the Arabian Sea found elevated organic ligand concentrations in the ODZ and noted the high conditional binding strengths (log $K^{cond}_{FeL,Fe'}$) of these ligands (Hopkinson and Barbeau, 2007; Kondo and Moffett, 2015; Witter et al., 2000). It has been hypothesized that the high ligand concentrations and strong stability constants in low oxygen regions result from the increased remineralization of organic matter, which is suspected to be a source of ligands (Boyd and Ellwood, 2010; Witter et al. 2001). Hopkinson and Barbeau (2007) suggested that the strong ligands observed in the ODZ are potentially the result of ligand production by organisms living in low oxygen regimes, some of which may have high iron requirements (e.g. Saito et al., 2020). However, the source of these ligands and the specific roles they play in Fe biogeochemistry in the ODZ environment remain elusive, largely because ligand identities are unknown. Recent advances in liquid chromatography coupled to inductively coupled plasma mass spectrometry and electrospray ionization-mass spectrometry (LC-ICP/ESI-MS) have enabled the ability to identify Fe-binding organic ligands (Boiteau and Repeta, 2015; Mawji et al., 2011, 2008; Velasquez et al., 2011). These analyses target the identification of siderophores, or small Fe-binding ligands with extremely high Fe-binding affinities. Siderophores are thought to be most often produced by bacteria under Fe-limiting conditions as a competitive method of Fe acquisition and solubilization (Kramer et al., 2019). The stability constants of siderophores generally overlap with the conditional binding strengths of the L_1 class of natural ligands that have been broadly observed in the marine environment via voltammetric methods, and with the ligands found in previous studies in the ETNP ODZ (Glass et al., 2015; Gledhill and Buck, 2012; Hopkinson and Barbeau, 2007). This suggests the possibility of siderophores contributing to the ligand pool in this region, though their presence may be surprising given the generally high Fe concentrations. To our knowledge however, no organic ligand characterization analyses targeting siderophores have been performed in any ODZ environments to date. The presence of such strong ligands in ODZs may have important implications for Fe reactivity and bioavailability in these regions, and may also play a role in the off-shelf transport of Fe from coastal margins.

In this paper, we investigate the speciation of dFe_T in the ETNP ODZ to elucidate the complex processes impacting Fe biogeochemistry in this and other similar regions. We combine measurements of dFe_T, Fe(II) and organic Fe-binding ligands using both targeted mass spectrometry approaches and traditional voltammetric characterization of the organic ligand pool. Together, these approaches provide an important step forward in understanding the role and identities of organic ligands in ODZs, and the role of organic ligands in ODZ Fe biogeochemistry.

2. Methods

2.1 Sample Collection and Storage

Samples in this study were collected from two Lagrangian stations and one regular station in March and April 2012 aboard the R/V *Thomas G. Thompson*. Lagrangian stations were sampled by deploying a free-floating surface-tethered sediment net trap array and tracking the array for the duration of the station (5 days each) to ensure sampling of the same water mass. Samples were collected using 5 L Teflon-coated external-spring Niskin-type bottles (Ocean Test Equipment) mounted on a trace metal clean rosette (Sea-Bird Electronics). The trace metal rosette was lowered over the side of the ship on a Kevlar line and the bottles were preprogrammed to trip on the upcast at specified depths with an autofire module (Sea-Bird Electronics). The trace metal rosette was equipped with temperature, conductivity, and fluorescence sensors, while the ship's rosette was additionally equipped with oxygen and transmissivity sensors. Once on board, Niskin bottles were quickly retrieved and mounted on a rack within a positive pressure Class-100 clean van. Bottles were pressurized with filtered N_2 gas, and samples were filtered through acid-cleaned 0.2 μm Acropak 200 capsule filters (Pall Corporation). All sample bottles were cleaned according to GEOTRACES "cookbook" protocols (Cutter et al., 2017). Samples were collected in 250 mL low-density polyethylene bottles (LDPE) bottles (Nalgene) for total dissolved metals, 500 mL fluorinated LDPE bottles for speciation analyses, and Teflon bottles for Fe(II) measurements. Total dissolved Fe (dFe_T) samples were acidified to pH < 1.7 via the addition of trace metal grade HCl (Optima, Fisher) then stored for at least one month prior to analysis. Speciation samples were stored at -20°C until analysis in the lab. Nutrient samples were directly collected from the Niskin bottles deployed from the ship's CTD rosette and subsequently filtered through GF/F glass fiber filters and refrigerated prior to analysis.

2.2 O_2, Nitrate and Nitrite measurements

The ship's CTD was equipped with a standard Seabird oxygen sensor (SBE43) that was calibrated using Winkler titrations carried out during the first leg of the cruise. All CTD data was then corrected using this calibration. The limit of detection was ~1 μmol kg^{-1} and was frequently reached in the ODZ. A Switchable Trace Oxygen (STOX) amperometric microsensor was then used to make additional oxygen measurements in the ODZ (Revsbech et al., 2011, 2009; Tiano et al., 2014) to define the anoxic layer. Details on these measurements are explained in detail elsewhere (Tiano et al., 2014). NO_3^- and NO_2^- concentrations were measured following standard JGOFs (United Nations Educational Scientific and Cultural Organization, 1994) protocols onboard with a Technicon Autoanalyzer using the Griess-Ilosvay colorimetric method (Strickland and Parsons, 1972) modified from the Armstrong procedure (Armstrong et al., 1967). Briefly, NO_2^- in water samples was diazotized with sulfanilamide and reacted with N-(1-

naphthyl)-ethylenediamine to form an azo dye with a maximum absorbance at 540 nm. A spectrophotometer equipped with a 15 mm flow cell was used to measure absorbance and quantify NO_2^-. Samples for NO_3^- analysis were first passed through a cadmium column to reduce NO_3^- to NO_2^- then analyzed in the same manner. The NO_3^- concentration is defined as the excess of NO_2^- determined from the cadmium column method over the original NO_2^- measurement.

2.3 Reagents

All reagents were prepared in a HEPA-filtered laminar-flow space or a Class-100 clean room. All samples and standards for Fe(II) analysis were stored in acid-cleaned Teflon bottles. For Fe(II) measurements, a 0.004 mol L^{-1} luminol stock solution was prepared in a 4 mol L^{-1} NH_4 and 0.5 mol L^{-1} HCl (Optima, Fisher Scientific) with luminol sodium salt (Sigma Aldrich). The stock solution was diluted to a working solution concentration of 0.001 mol L^{-1} and the pH was adjusted to 10.25-10.34. Working solutions were stored in the refrigerator and were allowed to sit for a minimum of 10 hours prior to use. All luminol solutions were prepared in 1 L amber high-density polyethylene (HDPE) bottles (Nalgene). Ferrous sulfate (Sigma Aldrich) was dissolved in pH 2 MilliQ (Optima HCl, Fisher Scientific) to prepare a 0.01 mol L^{-1} Fe(II) primary standard solution. 100 nmol L^{-1} secondary solutions were then prepared daily by diluting the primary standard in pH 2 MilliQ. For total dissolved Fe analysis, a 0.1 mol L^{-1} ammonium acetate buffer was prepared using equivalent parts 0.1 mol L^{-1} ammonium hydroxide (NH_4OH; Optima, Fisher Scientific) and 0.1 mol L^{-1} acetic acid (CH3COOH; Optima, Fisher Scientific). Nitrilotriacetatic acid (NTA) Superflow chelating resin (Qiagen) was cleaned and conditioned prior to use according to Lee et al. (2011). Briefly, the NTA resin (25 mL) was first washed five times with MilliQ, followed by five washes of 1.5 mol L^{-1} trace metal grade HCl (Optima, Fisher Scientific), concluding with several more MilliQ washes to ensure the removal of HCl from the solution. Following cleaning, the resin was then conditioned with 0.5 mol L^{-1} trace metal grade HCl and refrigerated for 4-5 days at ~4ºC. As a final cleaning step, the resin was then washed five times with 0.5 mol L^{-1} trace metal grade HNO_3 (Optima, Fisher Scientific) and five times with MilliQ water to ensure removal of HNO_3. The resin was then diluted two-fold with 25 mL MilliQ and stored in the refrigerator as the primary resin. Working resin suspensions were prepared using a 1:50 dilution of primary resin to MilliQ. All voltammetry reagents (salicylaldoxime, boric acid buffer, and Fe standards) were prepared in acid-cleaned Teflon bottles. A 4 mmol L^{-1} salicylaldoxime (SA) solution was prepared by dissolving SA (Fluka, > 98% assay) in methanol (CH_3OH, Optima Fisher). Boric acid (Alfa Aesar, 99.99% metals basis) was dissolved in 0.4 N NH_4OH (Optima, Fisher) to prepare a 1.5 M boric acid buffer. A 2 mM Fe primary standard was prepared by diluting Fe AA standard with pH 2 MilliQ. Four secondary Fe standards were made from the primary standard to final concentrations 100 nmol L^{-1}, 200 nmol L^{-1}, 1µmol L^{-1}, and 2 µmol $^{L-1}$ in pH 2 MilliQ.

2.4 Fe(II) Measurements

Fe(II) concentrations were determined shipboard using a luminol-based chemiluminescence technique adapted from (King et al., 1995) and modified according to Vedamati et al., (2014). An FeLume flow injection analysis (FIA) system (Waterville Analytical) was set up in continuous flow mode (see Hopkinson and Barbeau, 2007; Kondo and Moffett, 2013) such that sample and luminol were mixed at a constant 1:1 ratio in the flow cell. Both the luminol and sample were maintained at a pH between 10.25 and 10.34. The FIA system was calibrated using Fe(II) standard additions (0.5-1 nmol L^{-1}) to seawater taken at depth and stored for several days

in the dark. The detection limit, defined as 3 times the standard deviation of blank seawater measurements (n = 3), was 16 pmol L^{-1}. All Fe(II) measurements were completed immediately after sampling to avoid oxidative loss of Fe(II).

2.5 Total Dissolved Fe Analyses

Using a method adapted from (Lee et al., 2011), dFe_T concentrations were determined using a single batch NTA resin extraction followed by isotope dilution and subsequent ICP-MS analysis on an Element 2 (Thermo Scientific). Samples were prepared in 15 mL polypropylene (VWR) acid-cleaned tubes. Prior to analysis, tubes were rinsed seven times with MilliQ and at least once with the sample. Tubes were filled with ~7.5 mL sample (exact volume determined gravimetrically) and spiked with a sufficient ^{57}Fe-enriched spike (BDH Aristar Plus, VWR) to bring the final [^{57}Fe] to ~1 nM (exact concentrations were calculated using the gravimetrically determined volume for each sample). The pH was increased to at least 4 with the addition of 1.5 mL of 0.1 mol L^{-1} ammonium acetate buffer (Lee et al., 2011). For the dFe_T measurements, 0.1 mL of 1.5 mol L^{-1} trace metal grade hydrogen peroxide (Optima, Fisher Scientific) was also added to each sample (Lohan et al., 2005). Samples were then left to equilibrate for at least an hour at room temperature to ensure the complete oxidation of Fe(II) to Fe(III) (Lee et al., 2011).

Following equilibration, 200 µL of the working resin suspension was added to each sample and the tubes were placed on a shaker for 4-5 days. The samples were then centrifuged for 10 min at 4000 rpm, and the seawater was carefully decanted to leave only the resin beads at the bottom. The beads were washed with 3 mL MilliQ to remove salts and the tubes were once again centrifuged using the same settings. This step was repeated twice more to ensure total salt removal. After the final wash, 1 mL of 5% HNO_3 (Optima, Fisher Scientific) was added to each tube and samples were left on the shaker for 1-2 days, after which they were centrifuged and the carefully decanted sample was ready for analysis.

The isotope ratio (^{56}Fe:^{57}Fe) was determined on an Element 2 in medium resolution mode. Procedural seawater blanks were prepared the same way using ~0.2 mL low-metal surface seawater from the 2009 Pacific GEOTRACES intercomparison cruise. All samples were analyzed in triplicate. The Sampling and Analysis of Iron (SAFe) reference standards S1 and D1 (Johnson et al., 2007) were measured alongside the samples to assess the accuracy of the method. The resulting concentrations were 0.091± 0.007 nmol L^{-1} (n = 3) and 0.595 ± 0.029 nmol L^{-1} (n = 3) for S1 and D1, respectively. These values are within the range of consensus values for S1 (0.093 ± 0.008 n nmol L^{-1}) and somewhat lower than D1 consensus values (0.67 ± 0.04 nmol L^{-1}); http://www.geotraces.org/science/intercalibration).

2.6 Organic iron-binding ligands analyses

2.6.1 Voltammetric determination of the ligand pool

Competitive ligand exchange adsorptive cathodic stripping voltammetry (CLE-ACSV) was used to determine the concentration and strength of natural Fe-binding organic ligands. The theory is described in detail elsewhere (Abualhaija and van den Berg, 2014; Rue and Bruland, 1995). Briefly, an artificial ligand, in this case salicylaldoxime (SA), of known Fe-binding and equilibrium properties was added to samples to compete with the natural ligands. The Fe(SA) complex is electroactive and adsorbs onto the mercury drop during the deposition step. Then, a voltammetric signal is generated proportional to the amount of Fe that is stripped from the

surface of the mercury drop during a linear cathodic voltage sweep. By titrating the sample with increasing Fe at a constant artificial ligand concentration, the concentration and binding strengths of natural ligands can be calculated via chemical equilibria and mass balance. We assume that all dFe_T in the samples is exchangeable with SA over the timescale of equilibration (overnight), although we acknowledge that some species of particularly strong ligands or inorganic colloids may not be consistent with this assumption. In addition, all dFe_T was assumed to be present as Fe(III) because samples were collected and stored under oxic conditions; any Fe(II) present would have oxidized prior to the time of analysis.

For CLE-ACSV analyses, 15 separate 10 mL aliquots of each sample were transferred to acid-cleaned and conditioned Teflon vials (Savillex Corporation). Each aliquot was buffered to a pH of 8.2 (NBS scale) via addition of 50 µL of 1.5 mol L^{-1} boric acid-ammonia buffer. 25 µL of 4 mmol L^{-1} SA was pipetted into each aliquot for a final concentration of 10 µmol L^{-1}. Linear Fe additions were added to the aliquots ranging from 0 to 10 nmol L^{-1}. Samples were equilibrated overnight prior to analysis on a BASi hanging mercury drop electrode with a platinum auxiliary electrode and Ag/AgCl reference electrode (Bioanalytical Systems Incorporated). Samples were analyzed using differential pulse stripping voltammetry with a linear sweep of 0 to -800 mV, following a deposition step of 120 s at 0 volts (with stirring), and 15s of quiet time. Peak heights were calculated in ECD-SOFT using a curved baseline and ligand concentrations and strengths were then fitted using ProMCC (Omanović et al., 2015). The conditional stability constants used were $\log K^{cond}_{FeSA,Fe'} = 6.5$ and $\log B^{cond}_{FeSA_2,Fe'} = 10.2$ for the respective mono and bis complexes of SA, along with an inorganic side reaction coefficient $\log \alpha_{Fe'} = 10$ (Abualhaija and van den Berg, 2014). The conditional stability constants refer to the binding strength of Fe to SA relative to inorganic Fe (Fe′) while $\alpha_{Fe'}$ refers to the relative abundance of inorganically complexed Fe to free Fe. Only one ligand class was detected in the samples, based on visual inspection and error analysis in ProMCC. An initial internal sensitivity was calculated using the last 3 points of the titration curve and then adjusted based on visual inspection of the data.

2.6.3 Characterization of the ligand pool with mass spectrometry

In order to determine the identity of the Fe-binding organic ligands, the organic matter in our samples was extracted using solid phase extraction techniques followed by mass spectrometric analysis. To provide sufficient volume for these analyses, samples were pooled from the volume remaining from the voltammetric samples, resulting in pooled sample volumes ranging from 750 – 1650 mL. Samples were pooled according to 7 groups named for their location and average depth: LS1-33m, S107-137m, S107-325m, LS2-85m, LS2-350m, LS2-600m, and LS2-1217m. A MilliQ process blank was also extracted and analyzed to account for potential bottle effects from fluorinated LDPE bottles. To extract organic molecules from our samples, Bond-Elut ENV solid phase extraction (SPE) columns (1000 mg, 6mL; Agilent Technologies) were activated with 2 column volumes of distilled MeOH and rinsed with two column volumes of MilliQ prior to use. The pooled samples were then pumped onto the SPE columns and columns were then rinsed with MilliQ for 2-3 minutes following sample extraction to remove salts. Following preconcentration, columns were frozen at -20°C until analysis. Columns were later thawed and eluted using 13 mL of distilled or Optima grade methanol into acid-cleaned 15 mL falcon tubes. Sample extracts were dried down on a Speed-Vac concentrator (Thermo Scientific) system to ~0.5 mL and frozen until analysis. Extracts were weighed to determine extraction volume.

To identify organic ligands in our extracts, the samples were analyzed via liquid chromatography coupled to electrospray ionization mass spectrometry (LC-ESI-MS). Samples were injected and separated on a polyetheretherketone (PEEK)-lined C18 column using a Dionex Ultimate 3000 RSLCnano system in nanopump mode. We used a 5 mmol L^{-1} ammonium formate dissolved in both distilled methanol (solvent B) and in MilliQ water (Solvent A) gradient with a flow rate of 50 µL/min. The gradient starts at 5% B for 1 minute, followed by a 20 minute ramp from 5% to 90% B, then a 10 minute isocratic elution at 90% B, a 5 minute ramp from 90% to 95% B, a 5 minute isocratic elution at 95% B, before an 11 minute column conditioning step of 5% B for a total run time of 52 minutes. The LC flow was connected directly to a Q-Exactive HR mass spectrometer (Thermo Scientific). The sample was introduced using a HESI ion source with spray voltage of 3.5 kV, temperature of 320 °C, sheath gas of 16, sweep gas of 1, and auxiliary gas of 3 (arbitrary units). The auxiliary gas heater was set to 90 °C, and the S-lens RF level to 65.0. Scans were collected in positive ion mode with a *m/z* range of 200-2000 at 120,000 resolution and a maximum injection time of 50 ms. High-energy collision-induced dissociation MS^2 data were collected at 30,000 resolution targeting the most abundant ions and specific known siderophores (Baars et al., 2014) with an inclusion list using an isolation window of 1.0 m/z. A collision energy of 35% was used for fragmentation.

2.6.4 Siderophore identification

The LC-ESI-MS data were analyzed using an in-house R-code modified from that of Boiteau et al. (2016) and Bundy et al., (2018). First, ESI data was converted to an open source format (mzXML) using MS Convert (Proteowizard). The ESI-MS data was then mined for "targeted" compounds using a database of more than 300 known siderophores (Baars et al., 2014). Extracted ESI traces corresponding to the masses of the unbound "apo" form, ^{54}Fe form, and ^{56}Fe-bound form of each siderophore were then plotted for visual inspection. Only siderophores showing aligned peaks for all three forms were considered as putatively identified siderophores. Putative siderophores were then further examined based on MS^2 fragmentation data. Only putative siderophores with available MS^2 data and consistent fragmentation patterns across samples were continued to be considered putative siderophores. MS^2 spectra were compared to the literature when possible, but fragmentation data is often unavailable for these compounds. In the absence of existing MS^2 data, and to increase our confidence in the putative identification, in-silico fragmentation experiments were also performed on the likely siderophore candidates using publicly available CFM-ID 3.0 (https://cfmid.wishartlab.com).

3. Results

3.1 Regional Hydrography

Two Lagrangian stations (*see section 2.1*) were examined in this study: one coastal near shore station (LS1) and an offshore station (LS2) (Fig.1a). Two casts from an additional station (S107) were also examined (Fig.1a). LS1, located 40 km off of the Southwestern coast of Mexico, was primarily influenced by warm (~21 ºC), high-salinity (~35) Subtropical Underwater (STUW) at depths below 20 m, while surface samples were dominated by high-temperature (> 24ºC), relatively salty (> 34) Equatorial Surface Water (ESW) (Fig. 1b). The oxygen deficient layer, as defined by $[O_2] < 2$ µmol kg^{-1}, spanned from 35 m to 800 m depth in the nearshore LS1 (Fig. 1c). A primary NO_2^- maximum of 4.9 µmol kg^{-1} was detected at the top of the oxygen deficient layer (50 m), and a secondary maximum of 4.9 µmol kg^{-1} occurred at 150 m depth (Fig. 1e). The surface chlorophyll maximum (2.5 µmol kg^{-1}) was observed along with a secondary chlorophyll

maximum (15.7 μmol kg^{-1}) at 15 m (Fig. 1e). S107 was located 5 km Northeast of LS1 and shared similar features. STUW dominated below 20 m at S107, while ESW was the dominant water mass in the surface (Fig. 1b). The oxygen deficient layer at S107 stretched from 50 m to 800 m and contained a single NO_2^- maximum of 6.2 μmol/kg at 100 m along with a single chlorophyll maximum (14.1 μmol kg^{-1}) at 10 m (Fig. 1c,d). LS2 was located approximately 400 km offshore and slightly southwest of the nearshore stations. STUW dominated below 50 m, while surface waters were influenced by a band of high-temperature (> 25°C), low-salinity (< 34) Tropical Surface Water (Fig. 1b). The oxygen deficient layer at LS2 began at 100 m and extended to 800 m, and the primary NO_2^- maximum was located at 65 m (1.6 μmol kg^{-1}), and the secondary NO_2^- maximum (6.0 μmol kg^{-1}) was present at 150 m (Fig. 1c,f). The chlorophyll maxima were present at 60 m (3.0 μmol kg^{-1}) and at 110 m (3.6 μmol kg^{-1}; Fig. 1f). All three stations are dominated by STUW below 50 m depth and share identical oxygen profiles below 100 m depth.

3.2 Dissolved Iron and Iron Speciation

3.2.1 Dissolved iron distributions

The dFe_T at LS1 ranged from 1.42 nmol L^{-1} to 4.45 nmol L^{-1} with a prominent maximum at 30 m directly above the top of the ODZ, and a minimum of 1.42 nmol L^{-1} at 150 m coincident with the secondary NO_2^- maximum (Fig. 2a, 1e). Despite its close proximity to LS1, S107 had a much narrower range of dFe_T (1.08-1.48 nmol L^{-1}) and showed little to no change with depth (Fig. 2b). LS2 had dFe_T concentrations ranging from 0.62 nmol L^{-1} to 3.66 nmol L^{-1} with a primary dFe_T maximum of 2.06 nmol L^{-1} at 90 m coincident with the top of the ODZ and a secondary maximum of 3.66 nmol L^{-1} at 400 m (Fig. 2c). The dFe_T concentrations were found to be higher inshore at stations LS1 and S107 relative to the offshore LS2 station (Table 1). Offshore, average [dFe_T] was elevated in the ODZ relative to the oxygenated water column, while average inshore [dFe_T] was to be higher in the oxygenated region as a result of the primary dFe_T maximum at LS1 (Table 1). Although LS1 and LS2 were Lagrangian, there was considerable variability between casts (Fig. 2a,c), suggesting a dynamic environment. S107 did not exhibit noticeable variability between casts (Fig. 2b).

3.2.2 Fe(II) distributions

Fe(II) at LS1 had an Fe(II) maximum of 1.83 nmol L^{-1} at 30 m (range 0.01-1.83 nmol L^{-1}) (Fig. 2d), while LS2 had a maximum of 0.53 nmol L^{-1} at the surface and a secondary maximum of 0.16 nM between 150 and 200 m (range 0.06-0.53 nmol L^{-1}) (Fig. 2e). Unlike dFe_T, Fe(II) showed relatively little variability between casts at LS2. Fe(II) at LS1, however, exhibited similar variability between casts as dFe_T. The Fe(II) maximum at LS1 was coincident with the primary NO_2^- maximum, while the Fe(II) maximum at LS2 was coincident with the secondary NO_2^- maximum (Fig. 2d,e, Fig. 1e,f). Fe(II) was enriched in LS1 relative to LS2 for the majority of sampling depths. Similarly, the percentage of total Fe(II) (%Fe(II) = ([Fe(II)]/[dFe_T]) x 100) was higher inshore (range < 1 – 78%) compared to offshore (range 3 – 48%) for the majority of sampling depths (Fig. 2f). Below the Fe(II) maximum and within the ODZ (from 200-800 m at LS1 and 400-800 m at LS2), %Fe(II) remained relatively stable, averaging 10.2±2.4% for LS1 and 4.7±1.6% for LS2 (Fig. 2f). For both stations, %Fe(II) was greatest in the NO_2^- maxima. Fe(II) was not measured at S107.

3.3 Organic iron-binding ligand distributions and identities

3.3.1 Voltammetric determination of Fe-binding organic ligands

All samples contained a single ligand class whose concentration exceeded that of dFe_T at all sampling depths (Fig. 3), resulting in a pool of excess ligands ([eL] = [L] – [dFe_T]) throughout the water column. Although only a single ligand class was resolved per sample, the ligand binding strengths (log $K^{cond}_{FeL,Fe'}$) across the three stations ranged from a binding strength typical of the moderately strong L_2 class (log $K^{cond}_{FeL,Fe'}$= 11.0-12.0), to the strong L_1 class (log $K^{cond}_{FeL,Fe'}$> 12.0) based on the definitions suggested by Gledhill and Buck (2012) (Fig. 3). Samples from LS1, the station closest to shore, contained only L_1 type ligands (log $K^{cond}_{FeL,Fe'}$= 12.09-12.75) (Fig. 3g). S107 samples contained slightly weaker ligands (log $K^{cond}_{FeL,Fe'}$= 11.42-12.13), likely comprising a mixture of L_1 and L_2 ligands (Fig. 3h). Samples from LS2 also contained ligands with log $K^{cond}_{FeL,Fe'}$ spanning the range encompassed by both L_1 and L_2-type ligands (log $K^{cond}_{FeL,Fe'}$= 11.22-12.26). The strongest ligands at LS2 occurred within the oxygen deficient layer coincident with both elevated dFe_T and ligand concentrations (Fig. 3c, i).

Ligand concentrations ([L]) at LS1 (2.75-5.04 nmol L^{-1}), S107 (2.17-3.23 nmol L^{-1}), and LS2 (1.06-5.30 nmol L^{-1}) closely resembled the depth distributions for dFe_T (1.63-4.45, 1.08-1.49, 0.62-3.66 nmol L^{-1} respectively; Fig. 3a-c). Excess ligand ([eL]) at LS1 (0.52-1.61 nmol L^{-1}) and LS2 (0.17-3.13 nmol L^{-1}) displayed a maximum at the upper ODZ boundary, while [eL] at S107 (1.09-1.88 nmol L^{-1}) showed a maximum somewhat below the ODZ boundary (Fig. 3d-f). Table 1 describes ligand characteristics for four different environments: Inshore ODZ, Inshore Oxygenated, Offshore ODZ, and Offshore Oxygenated. Offshore station LS2 had higher average [L] in both the oxygenated and ODZ environments when compared to the corresponding inshore (LS1, S107) environments. Oxygenated areas had comparatively higher average [L] overall than their ODZ counterparts, but the [L] in the ODZ exhibited considerably more variability. Inshore [eL] were elevated in the oxygenated environment relative to the ODZ, while the opposite occurred offshore. The log $K^{cond}_{FeL,Fe'}$ similarly demonstrated opposing patterns inshore and offshore, with higher log $K^{cond}_{FeL,Fe'}$ values in the inshore oxygenated environment and lower log $K^{cond}_{FeL,Fe'}$ values in the offshore oxygenated environment relative to the corresponding ODZ values.

3.3.2 Characterization of the ligand pool using LC-ESI-MS

LC-ESI-MS analyses revealed the presence of identifiable siderophores, or Fe-binding organic ligands, in all samples. These samples were only searched for known siderophores, with a total of 3 putative siderophores being identified: Amphibactin B, synechobactin c9, and synechobactin c10. All samples contained one or more of the putatively identified siderophores (Table 2). The retention time and neutral losses corresponding with amphibactin B match those found in a suite of closely related amphibactins (Bundy et al., 2018). Synechobactin c10 displayed one matching fragment (*m/z* 288) to an existing published spectrum and a retention time close to that published using a similar experimental procedure (Boiteau and Repeta, 2015). In addition, good MS^1 peak alignment for the three forms of synechobactin c10 (Fe-free "apo" form, ^{54}Fe-bound, and ^{56}Fe-bound) was demonstrated in all samples containing this putative siderophore. Based on similar MS^1 peak alignment, we also putatively identified synechobactin c9 but MS^2 spectra were inconclusive.

Due to limited sample volumes, we were unable to quantify the identified siderophores using LC-ICP-MS as in previous work (Boiteau et al., 2013; Bundy et al., 2018). Instead, siderophore relative abundances are expressed in terms of the intensity (peak height) of the MS^1 peak normalized to sample volume (Table 2, Fig. 4). Amphibactin B was detected in LS1-33 m, S107-325 m, LS2-350 m and LS2-1217 m, which included environments both inshore and offshore, and within and outside the ODZ (Fig. 4). Synechobactin c10 was detected in LS1-33 m, S107-137 m, LS2-350 m, LS2-600 m, and LS2-1217 m. While synechobactin c10 did not have any apparent pattern inside or outside the ODZ, it had a higher relative abundance inshore (Fig. 4a). Synechobactin c9 was detected in all seven samples and its relative abundance increased with depth offshore (LS2) and peaked in abundance near the top of the ODZ inshore. No putatively identified siderophore demonstrated a distinct pattern based on oxygen concentrations. The small sampling volumes and the conservative definition of putative siderophores employed in this study suggest that these data are minimum estimates for the diversity of siderophores in this region.

4. Discussion

4.1 Dissolved iron dynamics inside and outside the ODZ

Both dFe_T and Fe(II) followed patterns typical in ODZ environments, with higher concentrations closer to shore and lower concentrations offshore (Johnson et al., 1997). The region was also highly dynamic, as evidenced by large differences between casts within a single Lagrangian station (Fig. 2). Comparisons of hydrography within a single Lagrangian station show no indication of changing water masses between casts. Therefore, the observed inter-cast variability is likely due to internal processes in the region, rather than an error in Lagrangian sampling. This is consistent with other observations from the ETNP, which also show a high degree of variability (K. Bolster pers. comm.). Both the dFe_T and Fe(II) displayed maxima at the top of the ODZ and near the NO_2^- max, which is consistent with other ODZ studies (Kondo and Moffett, 2015; Moffett et al., 2007). While the mechanisms producing the Fe maxima in the ODZ remain uncertain, possibilities include microbial Fe(III) reduction, remineralization of Fe on or incorporated into particles, or lateral advection from sediments (Kondo and Moffett, 2015; Vedamati et al., 2014). Although both Fe(II) and dFe_T displayed maxima in similar locations in the water column, the ratio of Fe(II) to dFe_T decreased offshore, suggesting the processes acting on the two Fe pools are decoupled (Fig. 3). Here, we address three hypotheses to explain the patterns between inshore and offshore seen in our study site, as well as the origin of the dFe_T and Fe(II) maxima within the top of the ODZ. The first hypothesis (1) is that Fe(II) is primarily produced *in situ* via reduction of the dFe_T pool. The second hypothesis (2) is that Fe(II) and dFe_T patterns in the ODZ are driven by remineralization of sinking organic matter. Finally, the third hypothesis (3) is that the majority of the observed Fe(II) and/or Fe(III) is released from the sediments and are gradually oxidized via inorganic or organic reaction pathways, biologically removed, or abiotically scavenged as waters are advected offshore.

According to hypothesis 1, if we assume *in situ* reduction of the dFe_T pool is the source of Fe(II), we would expect [Fe(II)] to be proportional to its [dFe_T] source. However, the Fe(II):dFe_T ratio decreased between the inshore and offshore stations. Furthermore, redox conditions in the ODZ were not sufficiently reducing to inorganically reduce Fe(III) to Fe(II) on a reasonable timescale, particularly in the presence of the known Fe oxidizers NO_2^-, NO_3^-, and organic ligands (Hopkinson and Barbeau, 2007). As such, any reduction of the dFe_T pool must be microbially

mediated. While anammox performing bacteria such as *Candidatus* Scalindua profunda demonstrate Fe(III) reduction in culture (Van de Vossenberg et al., 2013), the majority of known microbial Fe reducers are associated with anoxic sediments (Crosby et al., 2007; Thamdrup, 2000). It is possible that dFe_T is sourced from margin sediments and is slowly reduced as it is advected away from the margin, but due to the reducing nature of the sediments in this region it is more likely that a diffusive flux of dFe_T from sediments would be in the form of Fe(II). Therefore, it is unlikely that hypothesis 1 is the primary driver for the dFe_T and Fe(II) distributions observed in this study.

Hypothesis 2 is more difficult to address because we lack some important data in order to fully explore this hypothesis (e.g. particulate Fe and carbon measurements). However, evidence from isotope studies in the OMZ associated with the Senegalese margin found a heavy isotopic dFe_T signature, suggesting that remineralization is a significant processes in controlling dFe_T, particularly further away from the margin (Klar et al., 2018). To examine this mechanism, we used apparent oxygen utilization (AOU) as a proxy for remineralization. If the majority of dFe_T is being produced via remineralization, [dFe_T] should exhibit a positive linear correlation to AOU. Examination of this proxy indicated that AOU and dFe_T are correlated below the oxycline, and an alternative process must be driving dFe_T distributions at the surface. Below the oxycline, AOU can account for between 38% (LS1) and 74% (S107) of the variance in dFe_T (data not shown), suggesting that remineralization of organic matter provides an important, but variable source of dFe_T in the ODZ. AOU, however, cannot account for Fe(II) distributions. AOU exhibits no correlation to Fe(II) at LS1 and can only account for 28% of the variance in Fe(II) below the oxycline at LS2 (data not shown). Therefore, we propose that hypothesis 2 can partially explain vertical dFe_T distributions, but that remineralization of organic matter is unlikely to be the source of the observed Fe(II) distributions both within and above the ODZ.

Hypothesis 3 suggests that the majority of the Fe observed in this region, and particularly the reduced Fe, is advected offshore from reducing sediments within the ODZ. This hypothesis has been proposed in the ETSP, and several lines of evidence suggest its importance. Lam et al. (2020) found that advection offshore was responsible for Fe transport from the sediments to open ocean off the Peru margin particularly from the slope, but that much of the dFe_T was lost via precipitation. Heller et al. (2017) proposed that Fe(II) maxima in the ETSP ODZ arose from an advected sedimentary source, based on Fe and radium isotope patterns (Heller et al., 2017). Unfortunately, no isotopic data is available for the present study, but the offshore decrease in [dFe_T] and [Fe(II)] is consistent with an advected signal. In addition, the decreasing Fe(II):dFe_T ratio between inshore and offshore can be accounted for if we assume an initial sediment source for the two species and different rates of loss as they are advected offshore. The anoxic conditions in the ODZ would help to stabilize Fe(II) against oxidation, while conversely the high concentrations of strong organic ligands (such as siderophores) that we identified in the region would likely enhance Fe(II) oxidation. Additionally, the organic ligands present are expected to prevent Fe(III) from precipitating. The presence of inert colloidal forms of Fe(III), although not measured in this study, would also likely stabilize Fe(III) against precipitation. As such, we propose that Fe(II) released by the sediments (hypothesis 3) is the driving mechanism behind lateral changes in Fe(II) and dFe_T, while the vertical patterns of dFe_T in the two profiles are a result of remineralization (hypothesis 2). The vertical patterns in Fe(II) may also be primarily explained via hypothesis 3. The hypothesis governing horizontal variations in Fe distributions from inshore to offshore will be further explored in section 4.4 in the context of the observed

patterns in organic Fe-binding ligands, as the reactivity and redox behavior of Fe is likely strongly impacted by ligand processes in these coastal margins.

4.2 Evidence for in situ siderophore production in high Fe environments

The voltammetry results indicated that strong Fe-binding ligands are present both inside and outside the ODZ, based on the observed log $K^{cond}_{FeL,Fe'}$ (Fig. 3g,h,i). Strong L_1 Fe-binding ligands have been found throughout the global ocean, both in high and low Fe environments (Gledhill and Buck, 2012). The similar conditional stability constants of siderophores and L_1 ligands suggests that siderophores could possibly be present in many regions of the ocean. Siderophores were observed in all of our pooled samples from this work, despite the relatively high ambient dFe_T concentrations (Fig. 4). Siderophores are common in terrestrial soil environments (Baakza et al., 2004; Guerinot, 1994; Kraemer, 2004; Sandy and Butler, 2009), and one study found siderophores in the marine benthic boundary layer (Boiteau et al., 2019). The measured siderophores in our samples therefore may have been advected along with the Fe from coastal sediments, or they may have been produced *in situ*. However, the types of siderophores we identified suggest they were likely produced by microbes in the water column rather than advected from the reducing sediments. All three identified siderophores were amphiphilic, or containing a polar headgroup and fatty acid tail (Figure 4c). Amphiphilic siderophores are found almost exclusively in aquatic environments, where the tail is thought to anchor the molecule to the cell and prevent diffusive loss (Kramer et al., 2019). This contrasts to soil environments where diffusive loss is minimal and most local siderophores lack the fatty acid tail. The amphiphilic characteristics of the siderophores found in the ODZ therefore support active *in situ* production. *In situ* production of siderophores could be a result of high Fe requirements for organisms living in low oxygen environments (Saito et al., 2020), intense competition for Fe resources (Boiteau et al., 2016), or the presence of a relatively strong inert pool of FeL or particulate Fe such that siderophores are needed to access bioavailable Fe (Hogle et al. 2016; Bundy et al., 2018). Previous work shows that amphiphilic siderophores are generally found in regions where Fe is limiting, in contrast to suites of hydrophilic siderophores (not detected in this study) that have been found in more Fe-replete environments (Boiteau et al., 2016; Mawji et al., 2011). It is important to note, however, that the LC-ESI-MS method used to characterize siderophores is somewhat biased toward the detection of amphiphilic compounds based on the chromatography and solid phase extraction methods used (McCormack et al., 2003). As such, there remains the possibility of uncharacterized hydrophilic siderophores in this region. The presence of siderophores in our samples is perhaps surprising, and suggests there is either competition for Fe or Fe has limited bioavailability in this region despite its high total concentrations. Boiteau et al. (2019) noted that amphibactins in particular have only been found in environments with low [dFe_T] (<0.3 nmol L^{-1}) despite the presence of known amphibactin-producing bacteria in Fe-rich regions. The presence of amphibactin B in our samples therefore suggests that Fe stress might have triggered the production of this siderophore. Siderophore contribution to the ligand pool in ODZ environments may also contribute to the elevation in log $K^{cond}_{FeL,Fe'}$ values in this region. In addition, the oxidizing capacity of siderophores will result in rapid oxidation of Fe(II) despite low oxygen concentrations, thereby shortening the half-life of Fe(II) in the ODZ environment. The presence of such strong microbially-produced ligands in the ODZ has implications for Fe cycling and bioavailability in these important regions and will be important to explore further in future studies.

4.3 Distinct ligand characteristics in worldwide OMZs

Our data show that ligand strengths in the ODZ are stronger than those outside the ODZ in oxygenated waters (Fig. 3). The presence and likely *in situ* production of siderophores within the ODZ suggest that siderophores might be contributing to the elevated log $K'^{cond}_{FeL,Fe}$ observed. Although siderophores have not been previously measured in any ODZs or OMZs to our knowledge, a comparative examination of ligand parameters inside and outside of low-oxygen regions in other studies suggest that siderophores or other very strong ligands might be ubiquitous in these environments (Fig. 5). We chose to use OMZ regions for our comparative study as these data are more widely available than for ODZs. Data were compiled for the three largest permanent OMZs in the ocean: Arabian Sea (Witter et al., 2000), ETNP (present study, Hopkinson and Barbeau, 2007), and Eastern Tropical South Pacific (ETSP) (Buck et al., 2018; Kondo and Moffett, 2015). Additional results from two smaller OMZs, the Western Atlantic (Gerringa et al., 2015) and Cape Verde (Buck et al., 2015), were included as well. A summary of voltammetry variables for the seven studies used in the comparison can be found in Table 3. In order to compare regions, an oxygen cutoff of 20 μmol kg^{-1} was applied as the OMZ boundary for the three major OMZs, while the Western Atlantic OMZ was defined as depths ranging 150-1000 m (consistent with original paper) and the Cape Verde OMZ had a 40 μmol kg^{-1} oxygen cutoff. With the exception of the Arabian Sea, the data indicate that the average log $K'^{cond}_{FeL,Fe}$ could be stronger in low oxygen regions of the water column when compared to the oxygenated regions (Fig. 5). However, the relative changes in log $K'^{cond}_{FeL,Fe}$ ~~logK~~ between the two oxygen regimes are small enough that random variability in the ligand pool cannot be ruled out. The relatively small elevation in log $K'^{cond}_{FeL,Fe}$ might be expected for our siderophore hypothesis, however, because measured siderophore concentrations are typically low (~10 pmol L^{-1}) compared to the concentrations of the total ligand pool (1-5 nmol L^{-1}; Boiteau et al., 2016, 2019; Bundy et al., 2018). Even a small additional input of very strong ligands such as siderophores could plausibly be responsible for the slightly elevated log $K'^{cond}_{FeL,Fe}$ found in the majority of OMZ regions. It is important to note, however, that the studies compared here all use slightly different methods for characterizing the ligand pool (e.g. variation in analytical window and equilibration parameters), thereby making the comparison challenging. To address this, the analytical window and added ligand used by each study considered in this paper are reported in Table 4. The analytical window influences the type of ligands detected by CLE-ACSV, such that higher windows are more likely to capture strong ligands, while lower windows are more likely to capture weaker ligands (Bundy et al., 2014; Laglera and Filella, 2015). As such, caution must be applied when comparing studies performed under different analytical windows. While there is large variation in analytical window applied in the studies compared here, there is no correlation between the analytical window and log $K'^{cond}_{FeL,Fe}$. Furthermore, we compare log $K'^{cond}_{FeL,Fe}$ values within each study such that the analytical window is consistent for each oxygenated/OMZ pair (e.g. oxygenated log $K'^{cond}_{FeL,Fe}$ and OMZ log $K'^{cond}_{FeL,Fe}$ for Western Atlantic derive from same analytical window). Therefore, we conclude that the results are unlikely to be an artefact of CLE-ACSV methodological variation. An additional challenge in interpretation arises from variation in [dFe_T] between studies and oxygen conditions. While OMZs tend to have higher [dFe_T] than their oxygenated counterparts (Table 3), log $K'^{cond}_{FeL,Fe}$ for the compiled dataset shows no dependence on [dFe_T]. Therefore, log $K'^{cond}_{FeL,Fe}$ differences between oxygenated and OMZ regions cannot be attributed simply to dFe_T variation.

In addition to the subtle differences in log $K'^{cond}_{FeL,Fe}$ between OMZs and oxygenated environments, other distinct characteristics of the ligand pool were observed between regions in this work (Fig. 6). Apparent clusters in the ligand parameters were observed between the offshore and inshore ODZ, and the inshore and offshore oxygenated water column (Fig. 6). Overall though, the data exhibit trends consistent with data found in the majority of open ocean ligand studies (Caprara et al., 2016). While [dFe_T] in our study is higher than the majority of samples in the ligand database, log $K'^{cond}_{FeL,Fe}$ ~~logK~~ and [eL] still fall within the average range encountered for the majority of ligand studies (Fig. 6). This consistency suggests that ligands in the ODZ share fundamental similarities in terms of their composition and behavior to those in the rest of the ocean, despite the higher [dFe_T] environment. Thus, theoretical models about ligand cycling derived from open ocean samples can likely be broadly applied to the ODZ region. However, the four environments sampled in our study occupy distinct regions within the overall trend, suggesting subtle differences in their respective ligand pools. The environmental variation becomes important for addressing smaller-scale ligand dynamics and the role they play in regional Fe speciation. While it is important to acknowledge that biases in the CLE-ACSV technique could contribute to these small differences, the observed variation is potentially an indicator of ligand pool distinctions between environments that are worth exploring further.

4.4 Understanding the role of ligands in Fe cycling in the ODZ margin environment

The ligand pool in the ODZ margin environment has been shown to both have characteristics that are similar to other ligands present globally, and to also have unique features within the ODZ such as an elevated presence of particularly strong ligands, or siderophores. Previous work has explored Fe cycling in low oxygen regions largely in the context of inorganic redox processes, but this work has identified the potentially important role of ligands in facilitating off-shelf transport of dFe_T. To explore the impact of ligands on the observed Fe distributions and test the advection hypothesis (hypothesis 3), we developed a simple one-dimensional model of key processes involved in ODZ Fe speciation. The model is designed to predict changes in the speciation of Fe during lateral transport away from the shelf in the ODZ environment as a function of time. The model includes three species of Fe such that dFe_T = FeL + Fe′ + Fe(II) where FeL is organically-bound Fe and Fe′ is all inorganic species of Fe(III). These species are exchanged according to four major processes: oxidation of Fe(II), scavenging of Fe′, complexation of oxidizing Fe(II) by L, and biological uptake of FeL (Fig. 7a). Colloidal processes were omitted from the model, despite a possible role in dFe_T transport, because these data were not collected for this study. Additional processes (dust deposition and FeL reduction) were deemed insignificant on the timescale of interest and as such were left out. Vertical mixing processes were also omitted from the model in the interest of simplicity and a focus on lateral transport.

The model takes initial inputs of Fe(II) and FeL, the two dominant Fe species in this region based on the measurements of Fe(II) and the presence of excess ligands. Fe′ was excluded from the initial conditions because of its short residence time in the ODZ (~9-77 hrs; Witter et al., 2000) relative to transport offshore (~200 days, Margolskee et al., 2019) and its low concentrations in seawater (< 1% of [dFe_T]; Rue and Bruland, 1995). Therefore, initial FeL conditions were calculated as dFe_T – Fe(II) = FeL. Fe(II) oxidizes to Fe(III) in the model according to an adjustable half-life, $t_{1/2}$. Fe that leaves the Fe(II) pool as Fe(III) is partitioned into

either the FeL pool or the Fe′ pool according to an adjustable fraction, γ. The γ is a simplified proxy for the capacity of organic ligands to bind additional inputs of Fe(III), ranging from 0 (cannot bind any additional Fe(III)) to 1 (binds all additional Fe(III)). The large measured excess ligand (eL) concentrations and high binding strengths (log $K^{cond}_{FeL,Fe'}$) of the ligand pool in the region (Fig 3) indicate that most, if not all of the free Fe(III) should be immediately bound to ligands, therefore bringing the predicted γ closer to 1. However, the model allows for variation in γ to account for oxidation pathways that bypass the stage in which ligands can easily bind Fe(III) such that some Fe(III) may go into the Fe′ pool. Examples of this mechanism would be the formation of insoluble Fe(III) oxyhydroxides or nanoparticles. Any Fe(III) that is passed to the Fe′ pool is assumed to be scavenged and leave the dissolved phase (Heller et al., 2017; Liu and Millero, 2002). Fe(III) that enters the FeL pool is modified according to a biological uptake rate, η, that affects the entire FeL pool. Because FeL in the ODZ has a residence time on the order of 23-250 yrs (Witter et al., 2000), FeL decay is not considered an important sink in this model. The equations guiding this model are written recursively to facilitate more complex modifications in the future (e.g concentration dependent loss rates).

Equation 2:

$$\begin{cases} t_1 = 0 \\ [Fe(II)]_1 = [Fe(II)]_{init} \\ [FeL]_1 = [FeL]_{init} \\ t_n = t_{n-1} + 1 \\ [Fe(II)]_n = [Fe(II)]_{init} \times \left(\left(0.5^{\,t_n / t_{1/2}} \right) - \left(0.5^{\,t_{n-1} / t_{1/2}} \right) \right) + [Fe(II)]_{n-1} \\ [FeL]_n = [FeL]_{n-1} + [Fe(II)]_{init} \times \gamma \times \left(\left(0.5^{\,t_{n-1} / t_{1/2}} \right) - \left(0.5^{\,t_n / t_{1/2}} \right) \right) - \eta \end{cases}$$

The FeL and Fe(II) profiles from inshore station LS1 were used as inputs in the model and run for t = 5,000 hours to generate theoretical LS2 profiles. 5,000 hours is the predicted transport time from LS1 to LS2 based on modeled zonal velocities for the region (Margolskee et al., 2019). Results were depth-adjusted to account for deepening isopycnals offshore and then compared to the measured LS2 data. While it is unknown the extent to which LS1 and LS2 can be considered representative profiles of the region, they provide an important foundation for examining transport processes occurring there.

In order to test the hypothesis that Fe distributions can be explained by release of Fe from sediments within the ODZ combined with the oxidation of Fe(II) as waters were advected offshore, we tested different theoretical Fe(II) half-lives and compared the predicted profiles with the data (Fig. 7b). Half-life measurements for Fe(II) under several different ambient

conditions were used. Two theoretical half-lives measured under 30 nmol L^{-1} O_2 (Millero et al., 1987) and 30 µmol L^{-1} NO_3^- (Ottley et al., 1997) were compared with half-lives predicted from *in situ* measurements in the Peruvian OMZ (Croot et al., 2019). The theoretical half-lives for the 30 nmol L^{-1} O_2 and the 30 µmol L^{-1} NO_3^- experiments (16,000 hrs and 130,000 hrs respectively) were much longer than those predicted from *in situ* measurements (200-2,900 hrs). The shorter *in situ* half-lives suggest that something other than simple inorganic oxidation is occurring in ODZ environments. In our model, the 2,900 hour half-life was best able to predict the ODZ LS2 profile, consistent with *in situ* measurements in the ETSP and indicating the presence of additional oxidation pathways—possibly microbially-mediated Fe(II) oxidation or organic ligand-assisted oxidation. Above 200 m but still within the ODZ, a 1500 hr half-life best fits the LS2 profile, suggesting that Fe(II) in the upper part of the ODZ has an almost 50% shorter half-life compared to the heart of the ODZ, although it is still consistent with measured half-lives in the region (K. Bolster pers. comm.). This change in half-life is coincident with the onset of the oxycline and both the Fe(II) and dFe_T maxima. Additional factors that may be responsible for the predicted half-life discrepancy between upper and lower parts of the ODZ are pH and temperature. Cooler temperatures will result in slower Fe(II) oxidation, which is consistent with the slower half-life predicted for the deeper ODZ. Lack of pH measurements associated with our samples make it harder to account for this variable, but ODZs have lower pH, which will also slow Fe(II) oxidation, perhaps partially explaining the slower oxidation rates observed there (Millero et al., 1987).

The second stage of the model was to assign a reasonable FeL uptake rate, η (Fig. 7c) in order to test whether changes in Fe speciation during advection could be due to biological uptake of Fe. Although Fe uptake rates in ODZ environments are not well known, microbes in these regions are thought to have high Fe requirements compared to their counterparts in oxygenated regions (Glass et al., 2015; Hutchins et al., 2002). A range of FeL uptake rates were estimated based on literature values, and microbes were assumed to be able to access organically-bound Fe (FeL), but the mechanism was not specified. An Fe uptake rate measured in heterotrophic bacterial isolates under Fe-limiting conditions, 27 fmol Fe L^{-1} hr^{-1}, was established as the lower limit (Tortell et al., 1996). An upper limit of 500 fmol L^{-1} hr^{-1} was calculated using an average steady-state Fe uptake rate from six bacterial strains under Fe-limiting conditions, 3.37 x 10^{-23} mol Fe $cell^{-1}$ min^{-1} (Granger and Price, 1999) and applying the uptake rate to cell abundances found in the ETSP OMZ core (1-25 x 10^5 cells mL^{-1}) (Maßmig et al., 2020). An uptake rate of 200 fmol L^{-1} hr^{-1} generated the best modeled prediction of the LS2 profile as indicated by analysis of least squares of the predicted data compared to the observed profile.

In order to determine the impact of organic Fe-binding ligands on Fe speciation of the ODZ, the final stage of model testing was to examine the effects of the organic ligand pool on the observed FeL concentrations (Fig. 7d). This was done by adjusting the ligand binding capacity, γ, while maintaining the 2,900 hour Fe(II) half-life and a constant 200 fmol L^{-1} hr^{-1} FeL uptake rate, determined from the preceding model results. Variability in γ is used to reflect differences in ligand strength and concentration, as well as the manner by which Fe(II) is oxidized. For instance, Fe-oxidizing bacteria, known to reside in OMZs, oxidize Fe(II) and precipitate Fe(III) in the same step (Emerson et al., 2010; Scholz et al., 2016), thereby effectively sequestering the resultant Fe(III) from rapid ligand uptake. In addition, γ may also reflect pH variability in the region as lower pH values are associated with a lower ligand binding capacity. While γ

adjustments did not alter the predicted LS2 profile to the degree that the Fe uptake rate and Fe(II) half-life did, it did significantly change the proportion of the dFe_T that was comprised of [FeL]. At individual depths, the difference in FeL between γ=0 and γ=1 range from 0 to 1.3 nmol L^{-1}, changing the [FeL] by up to 60 % on average. Thus, changes to the ability of natural ligands to bind additional Fe inputs can have a large impact on the observed dFe_T. The effectiveness of ligand binding in the ODZ can therefore significantly impact the longevity, and potentially the ultimate bioavailability, of Fe sourced from margins within the ODZ. The ligand binding capacity, or γ, that best fit the measured profile changed with depth, suggesting a dynamic environment consistent with the inter-cast variability in dFe_T. Differences in γ, and by extension the ligand pool, may account for some of the observed variability in dFe_T. This was also supported by the Fe(II) profiles, since Fe(II) was unaffected by γ in our model, and the Fe(II) profiles were not nearly as variable as the dFe_T.

Overall, the simple model results (Fig. 7) demonstrated a reasonable qualitative and quantitative prediction of the offshore depth profiles below 200 m and within the ODZ, thereby suggesting that the simple Fe speciation in our model accounts for the major processes affecting dFe_T as waters are advected from the margin offshore. Although it is probable that many processes are occurring to some degree, our model indicates that advection and ligand-mediated oxidation of Fe(II) are among the driving forces behind the observed Fe distributions offshore. The facility with which ligands can complex this oxidized Fe(II) is likely key to understanding the transport efficiency of Fe from the margin offshore. Variability in the ligand pool is shown in the model to have a large impact on observed dFe_T, and, by extension, the efficiency of shelf to offshore Fe transport. When examining characteristics of the ODZ ligand pool, analysis of log $K^{cond}_{FeL,Fe'}$ differences between oxygenated and OMZ regions (*section 4.3*) suggests the presence of a "background" ligand pool in the ODZ that is similar to ligands globally. This is supported by the similarities between this study's dataset and the global ligand database (Fig. 6) and suggests that the fundamentals of this model can be applied to other OMZ or nearshore environments. However, the log $K^{cond}_{FeL,Fe'}$ for ligands in the ETNP ODZ and other OMZ locations is consistently higher than that of corresponding oxygenated areas, possibly as a result of siderophore production in the low oxygen regions (Fig. 7). This manifests as an environmentally-specific ligand signature (Fig. 6) that could be a source of variability in the ligand pool as the production rates and residence times of siderophores are poorly constrained. Thus, small changes in the ligand pool, particularly in the strong ligand pool, may have large impacts on dFe_T transport.

5. Conclusions

Organic Fe-binding ligands play a fundamental role in Fe cycling in the ETNP ODZ. Our model shows that the degree to which ligands bind Fe after oxidation of Fe(II) modulates the size of the offshore dFe_T pool. Furthermore, based on the modeled half-life of Fe(II), it is likely that organic ligands facilitate Fe(II) oxidation, shortening its half-life from predicted inorganic oxidant based values. The identity of organic ligands in the ODZ has additional implications for Fe biogeochemistry in the region. Here, we present the first evidence for siderophore production in an ODZ environment. Their presence suggests the possibility of Fe competition in the ODZ, despite high ambient [dFe_T]. Siderophore production may also be a source of the stronger ligand signatures found in ODZs/OMZs relative to oxygenated areas, possibly elevating the average ODZ/OMZ ligand binding strengths beyond a universal background pool of ligands and increasing the longevity of dFe_T. Overall, the presence and composition of organic Fe-binding

ligands in the ETNP ODZ facilitate offshore Fe transport and can account for many of the observed patterns in dFe_T and Fe(II).

6. Acknowledgements

We thank the captain and crew of the R/V *Thomas G.Thompson* and Chief Scientist Allan Devol. Thank you to Rachel Horak and Carolyn Buchwald for nutrient analyses and to Yang Han for shipboard work. Thank you to Charles C. Lanfear for assistance in coding the model. We also thank Joe Resing and Kenny Bolster for their helpful comments on the manuscript. This work was supported by NSF-OCE #1029316 to Allan Devol and NSF-OCE #1756402 to Laura Moore and Randelle M. Bundy.

7. Author Contributions

LM performed ligand measurements and analyses, developed the model and drafted the manuscript. RB designed study, performed shipboard analyses and helped draft the manuscript. MH wrote Fe analysis and sampling methods, performed dFe_T and Fe(II) analyses, and commented on the manuscript. JM and KB commented on the manuscript.

Figure Captions

Figure 1: (a) Station Map. The three major stations are LS1 (red) located 40 km off of the Mexican coast, S107 (yellow) located 5 km Northeast of LS1, and LS2 (blue) located 400 km off of the Mexican coast. **(b)** Temperature-Salinity plot for S107 (black), LS1 (red), and LS2 (blue). **(c)** Oxygen profiles for S107 (black), LS1 (red) and LS2 (blue). Inset zooms in on upper 100 m. **(d-f)** Nitrite (purple) and chlorophyll (green) profiles for LS1 (d), S107 (e), and LS2 (f).

Figure 2: (a-c) dFe_T profiles at LS1 (a), S107 (b), and LS2 (c). Line styles and symbols refer to different casts in a Lagrangian station. Grey bars denote ODZ boundaries. **(d, e)** Fe(II) profiles for LS1 (d), and LS2 (e). Fe(II) was not collected for S107. Line styles indicate different casts in a Lagrangian station. Grey bars denote ODZ boundaries. **(f)** Fe(II) : dFe_T ratio for LS1 (purple) and LS2 (green).

Figure 3: (a-c) dFe_T (red) and L (purple) profiles at LS1 (a) S107 (b) and LS2 (c). **(d-f)** Excess ligand ([eL] = [L] – [Fe]) profiles at LS1 (d), S107 (e) and LS2 (f). **(g-i)** Ligand binding strength (log $K^{cond}_{FeL,Fe'}$) profiles at LS1 (g), S107 (h), and LS2 (i). Grey bars denote ODZ boundaries.

Figure 4: Siderophore abundances at inshore stations **(a)** and offshore stations **(b)**. Abundance is calculated as the height of the MS[1] peak corresponding to the siderophore. Grey bars denote ODZ boundaries. **(c)** Synechobactin c9, c10 structures. **(d)** Amphibactin B structure.

Figure 5: Comparison of ligand binding strengths (log $K^{cond}_{FeL,Fe'}$) between oxygenated and oxygen deficient portions of the water column for seven different OMZ studies, including: Two studies from the ETNP (this study; magenta, and Hopkinson and Barbeau; green), two studies from the ETSP (Kondo and Moffett 2015; light blue, and Buck et al. 2018; yellow), an Eastern Atlantic (Cape Verde) study (Buck et al. 2015; blue), a Western Atlantic study (Gerringa et al. 2015; brown), and a study from the Arabian Sea (Witter et al. 2000; coral).

Figure 6: (a) Ligand binding strength (log $K^{cond}_{FeL,Fe'}$) plotted against excess ligand concentrations ([eL] = [L] – [dFe_T]). **(b)** log $K^{cond}_{FeL,Fe'}$ plotted against total iron concentration ([dFe_T]). **(c)** Total ligand concentration ([L]) plotted against [dFe_T]. Colors refer to sampling environment: yellow = offshore oxygenated, green = inshore oxygenated, blue = offshore ODZ, red = inshore ODZ. Grey symbols are from the compiled ligand database (Caprara et al., 2016).

Figure 7: (a) Model Scheme. **(b)** Variation in modeled Fe(II) offshore profiles as a function of half-life. Compared to measured LS2 profile (black). **(c)** Variation in modeled FeL offshore profiles as a function of FeL uptake rate, η. Compared to measured LS2 profile (black). **(d)** Variations in modeled FeL offshore profiles as a function of the ligand binding capacity, γ (the percent of oxidizing Fe(II) entering the FeL pool). Compared to measured LS2 profile (black).

847 Figure 1.

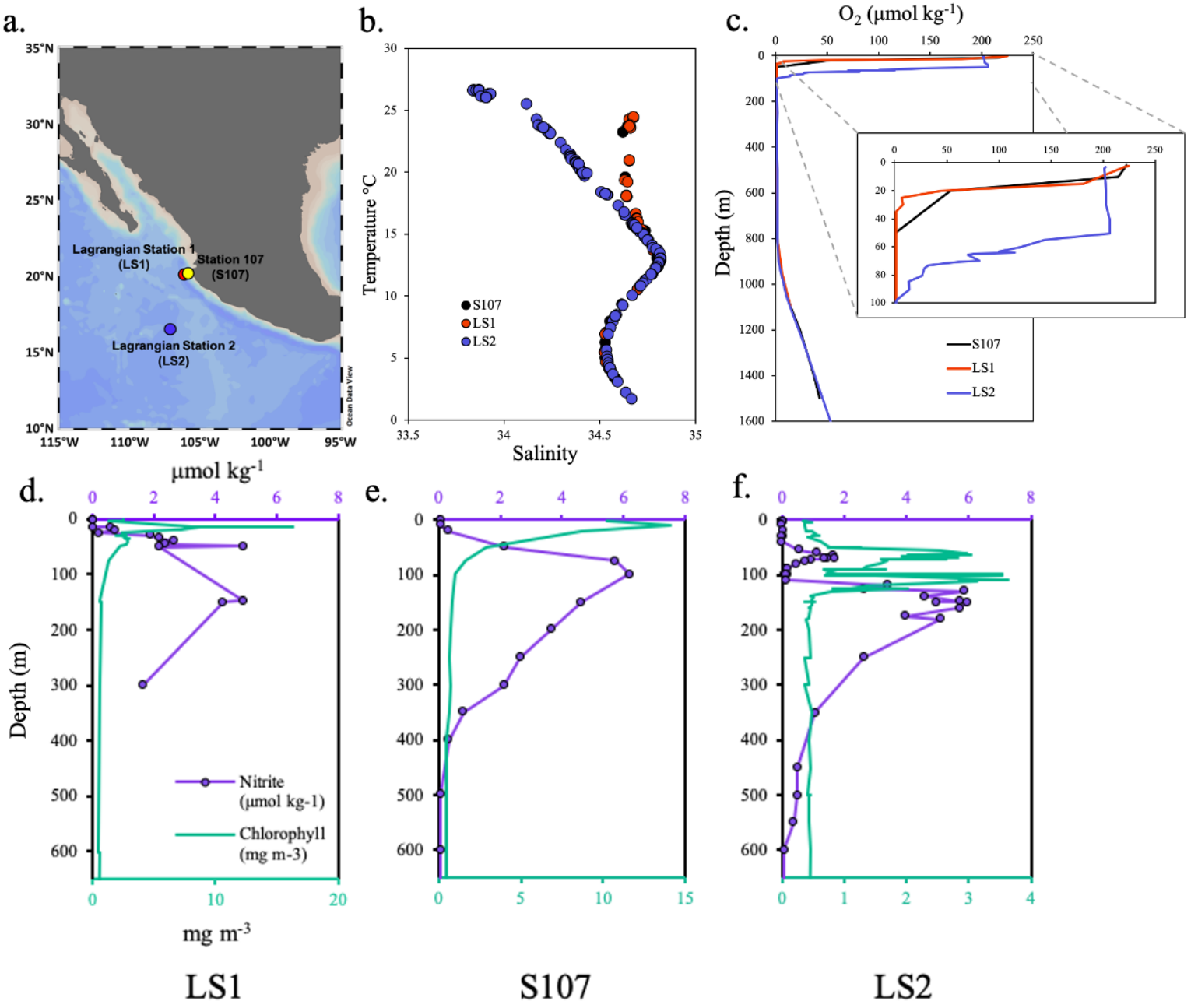
a.
35°N
30°N
25°N
20°N
15°N
10°N
115°W
110°W
105°W
100°W
95°W
Lagrangian Station 1
(LS1)
Station 107
(S107)
Lagrangian Station 2
(LS2)
Ocean Data View
b.
Temperature °C
Salinity
S107
LS1
LS2
c.
O2 (µmol kg-1)
Depth (m)
S107
LS1
LS2
d.
µmol kg-1
Depth (m)
Nitrite
(µmol kg-1)
Chlorophyll
(mg m-3)
mg m-3
e.
f.
LS1
S107
LS2

Figure 2.

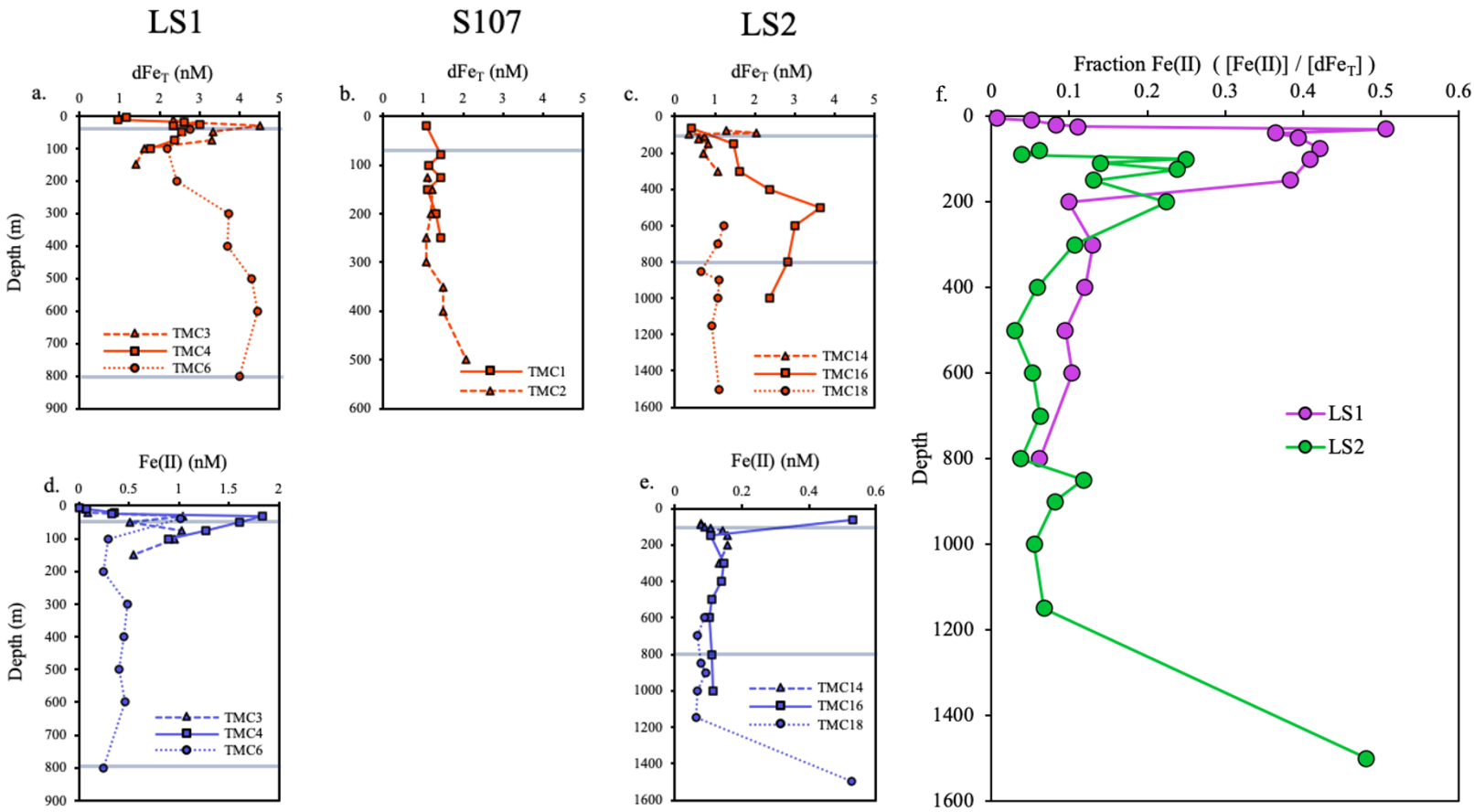
LS1
S107
LS2
a.
b.
c.
dFeT (nM)
Depth (m)
TMC3
TMC4
TMC6
TMC1
TMC2
TMC14
TMC16
TMC18
d.
e.
Fe(II) (nM)
f.
Fraction Fe(II) ([Fe(II)] / [dFeT])
Depth
LS1
LS2

Figure 3.

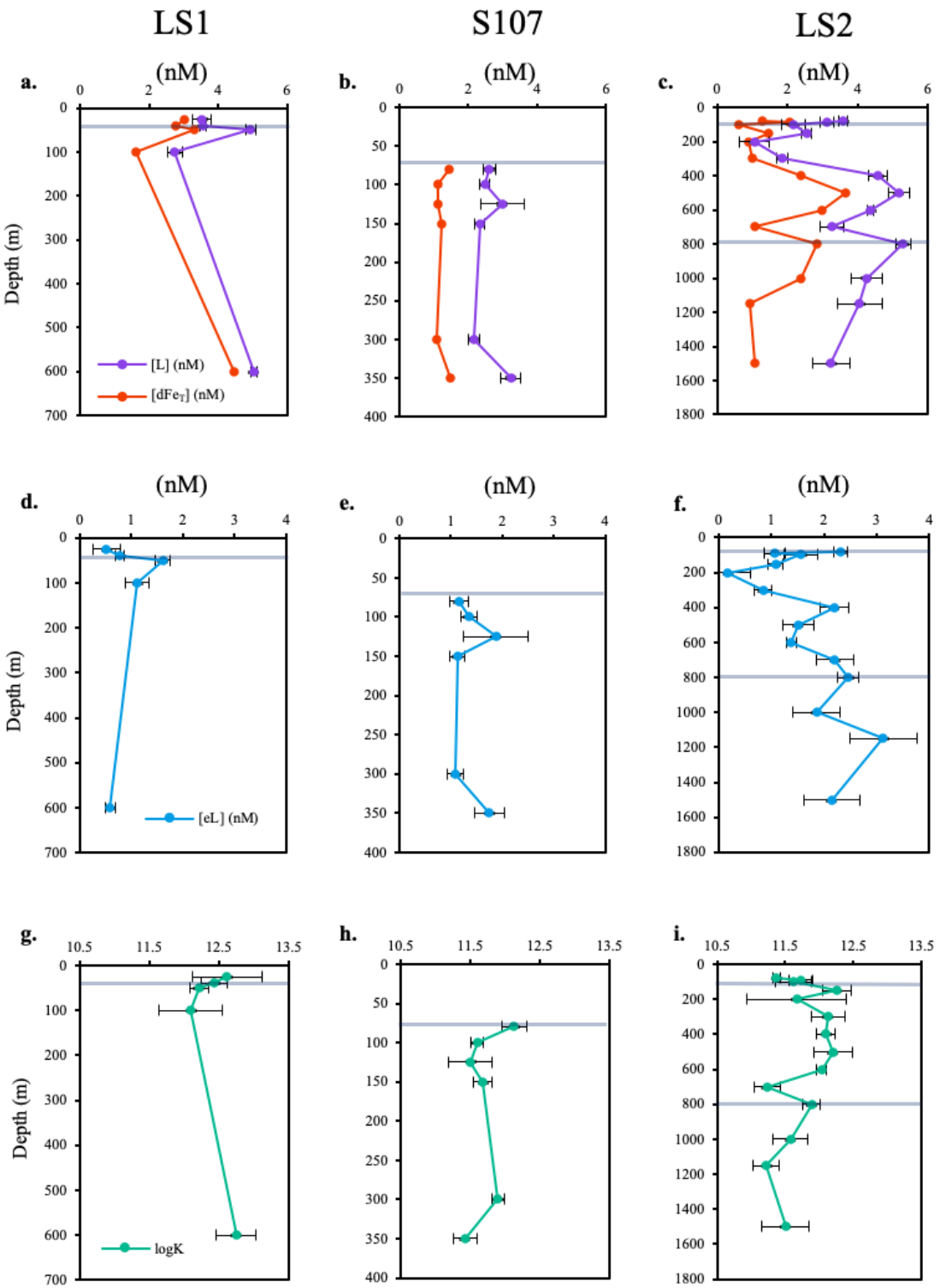

848 Figure 4.

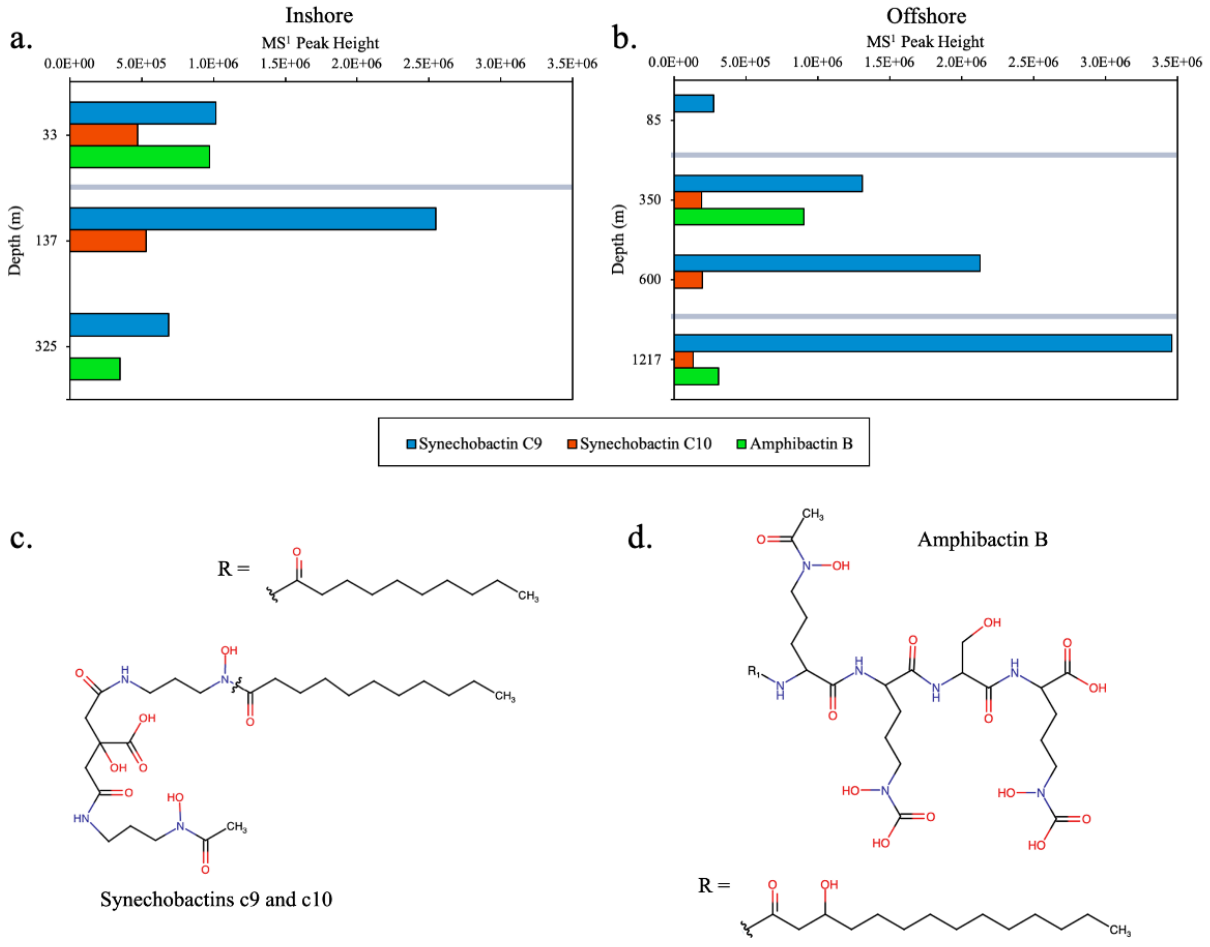

849

850 Figure 5.
851

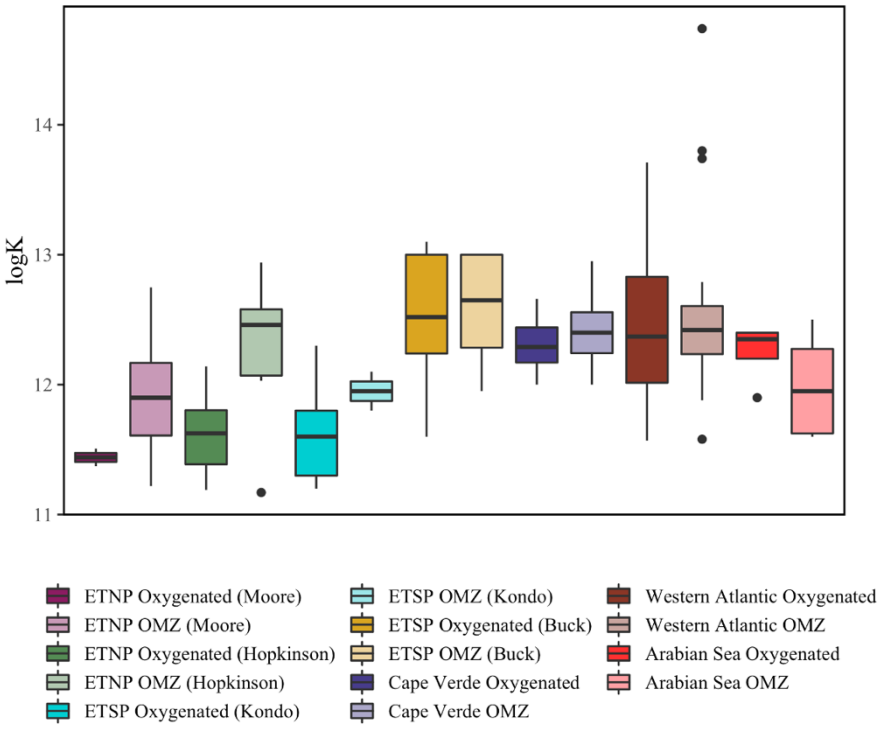

852 Figure 6.

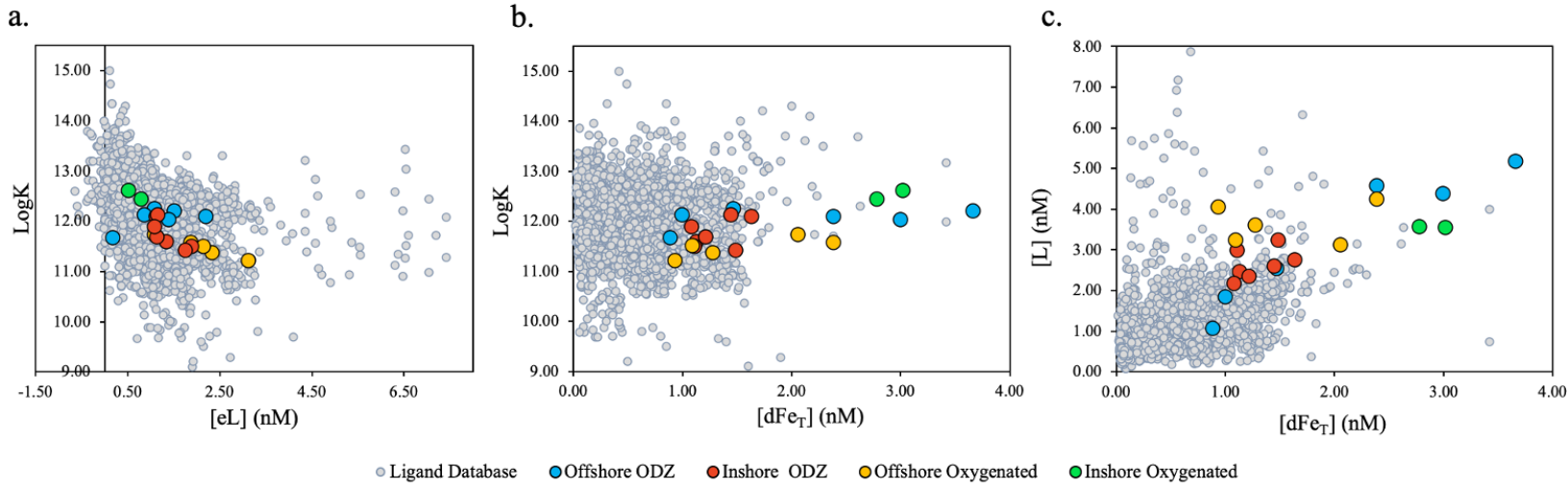
a.
b.
c.
LogK
[eL] (nM)
[dFe$_T$] (nM)
[L] (nM)
Ligand Database
Offshore ODZ
Inshore ODZ
Offshore Oxygenated
Inshore Oxygenated

853 Figure 7.

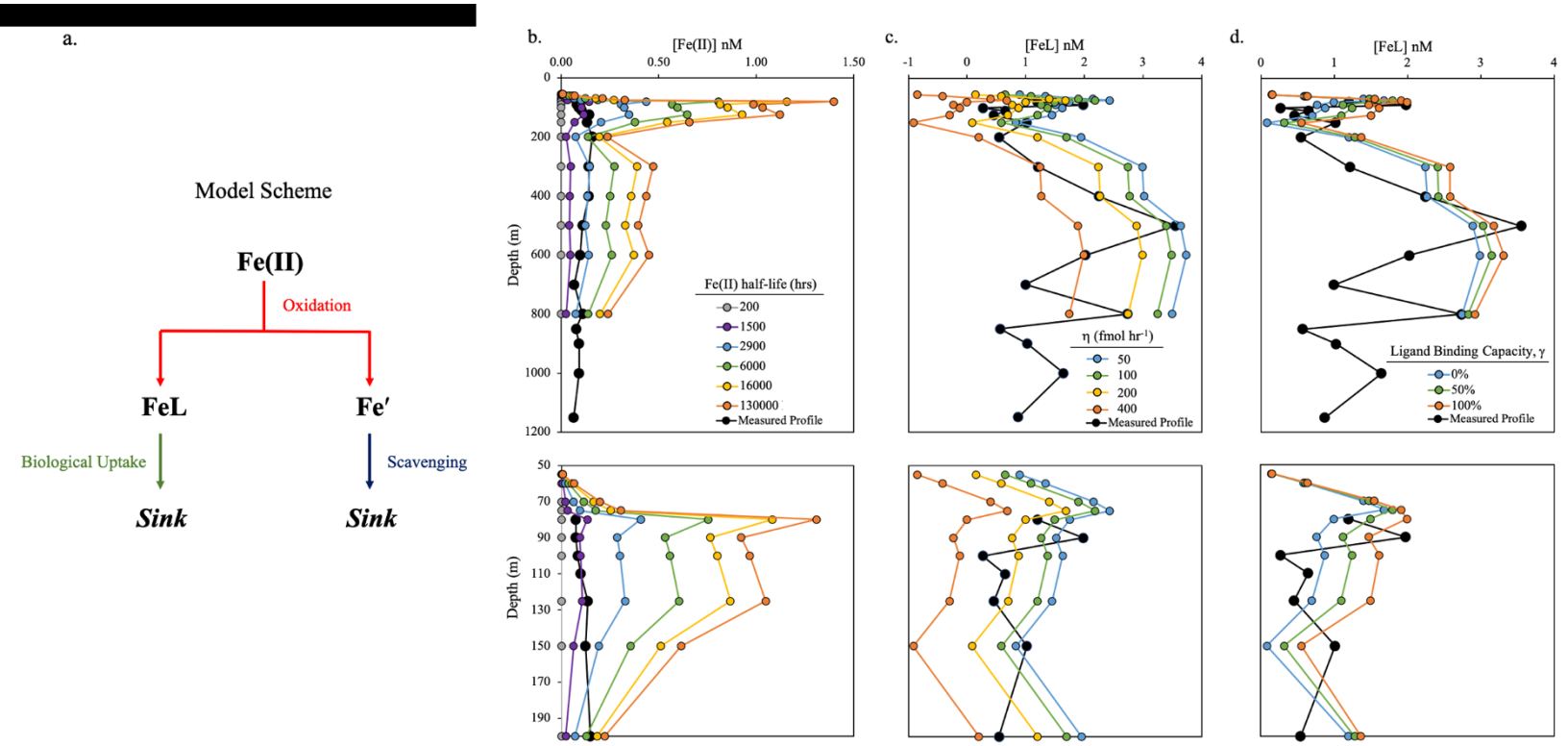
a.
Model Scheme
Fe(II)
Oxidation
FeL
Fe′
Biological Uptake
Scavenging
Sink
Sink
b.
[Fe(II)] nM
0.00
0.50
1.00
1.50
Depth (m)
Fe(II) half-life (hrs)
200
1500
2900
6000
16000
130000
Measured Profile
c.
[FeL] nM
-1
0
1
2
3
4
η (fmol hr-1)
50
100
200
400
Measured Profile
d.
[FeL] nM
0
1
2
3
4
Ligand Binding Capacity, γ
0%
50%
100%
Measured Profile

Table 1: Voltammetry data summary by sampling environment, including [dFe_T], [Fe(II)], [L], [eL], and log $K^{cond}_{FeL,Fe'}$. Errors are shown as ± 1 standard deviation.

	Inshore ODZ	**Inshore Oxygenated**	**Offshore ODZ**	**Offshore Oxygenated**
[dFe_T] (nmol kg^{-1})	2.93±0.98 (n=15)	2.45±1.11 (n=8)	1.54±1.04 (n=15)	1.09±0.51 (n=9)
[Fe(II)] (nmol kg^{-1})	0.69±0.41 (n=15)	0.47±0.64 (n=8)	0.12±0.03 (n=15)	0.18±0.20 (n=9)
[L] (nmol kg^{-1})	2.65±0.37 (n=7)	3.55±0.01 (n=2)	3.27±1.67 (n=6)	3.66±0.49 (n=5)
[eL] (nmol kg^{-1})	1.35±0.33 (n=7)	0.65±0.18 (n=2)	1.20±0.68 (n=6)	2.11±0.74 (n=5)
log $K^{cond}_{FeL,Fe'}$	11.76±0.28 (n=7)	12.53±0.13 (n=2)	12.07±0.21 (n=6)	11.48±0.20 (n=5)

Table 2: Siderophore identifications, with siderophore name, neutral mass, precursor ion, average retention time, apo peak mass (iron free), ^{56}Fe bound mass, and major MS^2 fragments.

Siderophore	**Neutral Mass (g/mol)**	**Precursor Ion ^{56}Fe monoisotopic $[M + H]^+$ *m/z***	**Retention Time (min)**	**Apo Mass *m/z***	**^{56}Fe mass *m/z***	**Dominant fragments *m/z***
Synechobactin C9	518.295	572.21	22.55	519.303	572.214	133.09, 205, 317.12, 361.07, 405.02
Synechobactin C10	532.311	586.23	27.03	533.318	586.229	117.07, 229.02, 289, 291.02, 307.01, 327.15
Amphibactin B	847.490	901.41	19.14	848.498	901.409	596, 624, 683

Table 3: Summary of voltammetry variables used in the interstudy comparison, including [dFe_T], [L], [eL], and log $K'^{cond}_{FeL,Fe'}$, ~~and α_L~~. Errors are shown as ± 1 standard deviation.

	Current study		**Hopkinson and Barbeau 2007**		**Kondo and Moffett 2015**		**Buck et al. 2018**		**Buck et al. 2015**		**Gerringa et al. 2015**		**Witter et al. 2000**	
	Oxygenated (n = 2)	*OMZ (n = 23)*	*Oxygenated (n = 8)*	*OMZ (n = 9)*	*Oxygenated (n = 8)*	*OMZ (n = 4)*	*Oxygenated (n = 77)*	*OMZ (n = 63)*	*Oxygenated (n=65)*	*OMZ (n=38)*	*Oxygenated (n = 54)*	*OMZ (n = 21)*	*Oxygenated (n = 4)*	*OMZ (n = 6)*
[dFe_T] (nmol L^{-1})	1.18 ± 0.13	1.95 ± 1.05	0.15 ± 0.08	0.80 ± 0.25	0.28 ± 0.46	0.70 ± 0.51	0.78 ± 0.64	1.36 ± 1.81	0.95 ± 0.38	1.26 ± 0.24	0.57 ± 0.29	0.80 ± 0.31	1.70 ± 0.63	1.74 ± 0.35
[L] (nmol L^{-1})	3.42 ± 0.25	3.37 ± 1.17	0.80 ± 0.31	1.13 ± 0.28	1.03 ± 0.48	1.20 ± 0.89	1.30 ± 0.77	2.30 ± 2.53	1.74 ± 0.45	1.84 ± 0.40	1.14 ± 0.38	1.36 ± 0.47	2.92 ± 1.64	4.48 ± 1.08
[eL] (nmol L^{-1})	2.24 ± 0.12	1.41 ± 0.68	0.65 ± 0.29	0.32 ± 0.31	0.75 ± 0.34	0.50 ± 0.50	0.52 ± 0.48	0.95 ± 0.92	0.79 ± 0.26	0.59 ± 0.30	0.57 ± 0.42	0.56 ± 0.52	1.22 ± 1.58	2.73 ± 1.13
log $K'^{cond}_{FeL,Fe'}$	11.44 ± 0.10	11.91 ± 0.41	11.62 ± 0.30	12.31 ± 0.54	11.66 ± 0.37	11.95 ± 0.13	12.55 ± 0.39	12.62 ± 0.36	12.30 ± 0.18	12.41 ± 0.22	12.44 ± 0.50	12.47 ± 0.52	12.25 ± 0.24	11.98 ± 0.40

863 Table 4: Summary of added ligands (identity and concentration) and analytical windows ($\alpha_{Fe'AL}$)
864 used by the studies in the log $K^{cond}_{FeL,Fe'}$, and α_L intercomparison. SA refers to salicylaldoxime,
865 TAC refers to 2-(2-Thiazolylazo)-p-cresol, and NN refers to 1-nitroso-2-napthol.
866

	Current study	Hopkinson and Barbeau 2007	Kondo and Moffett 2015	Buck et al. 2018	Buck et al. 2015	Gerringa et al. 2015	Witter et al. 2000
Added Ligand	SA	TAC	TAC	SA	SA	TAC	NN
Concentration Added Ligand (μmol L^{-1})	10	10	7.3	25	25	10	20
Analytical window $\alpha_{Fe'AL}$	33	250	134	60	60	250	1096
Added Ligand Equilibration Time	Overnight	1 hr	12 - 17 hrs	≥ 15 min	≥ 15 min	> 6 hrs	16 hrs

867

868
869
870 **References**
871
872 Abualhaija, M.M., van den Berg, C.M.G., 2014. Chemical speciation of iron in seawater using
873 catalytic cathodic stripping voltammetry with ligand competition against salicylaldoxime.
874 Mar. Chem. 164, 60–74. https://doi.org/10.1016/j.marchem.2014.06.005
875 Armstrong, F.A.J., Stearns, C.R., Strickland, J.D.H., 1967. The measurement of upwelling and
876 subsequent biological process by means of the Technicon Autoanalyzer® and associated
877 equipment. Deep. Res. Oceanogr. Abstr. 14, 381–389. https://doi.org/10.1016/0011-
878 7471(67)90082-4
879 Baakza, A., Vala, A.K., Dave, B.P., Dube, H.C., 2004. A comparative study of siderophore
880 production by fungi from marine and terrestrial habitats. J. Exp. Mar. Bio. Ecol. 311, 1–9.
881 https://doi.org/10.1016/j.jembe.2003.12.028
882 Baars, O., Morel, F.M.M., Perlman, D.H., 2014. ChelomEx: Isotope-assisted discovery of metal
883 chelates in complex media using high-resolution LC-MS. Anal. Chem. 86, 11298–11305.
884 https://doi.org/10.1021/ac503000e
885 Boiteau, R.M., Fitzsimmons, J.N., Repeta, D.J., Boyle, E.A., 2013. Detection of iron ligands in
886 seawater and marine cyanobacteria cultures by high-performance liquid chromatography-
887 inductively coupled plasma-mass spectrometry. Anal. Chem. 85, 4357–4362.
888 https://doi.org/10.1021/ac3034568
889 Boiteau, R.M., Mende, D.R., Hawco, N.J., McIlvin, M.R., Fitzsimmons, J.N., Saito, M.A.,
890 Sedwick, P.N., Delong, E.F., Repeta, D.J., 2016. Siderophore-based microbial adaptations
891 to iron scarcity across the eastern Pacific Ocean. Proc. Natl. Acad. Sci. U. S. A. 113,
892 14237–14242. https://doi.org/10.1073/pnas.1608594113
893 Boiteau, R.M., Repeta, D.J., 2015. An extended siderophore suite from Synechococcus sp. PCC
894 7002 revealed by LC-ICPMS-ESIMS. Metallomics 7, 877–884.
895 https://doi.org/10.1039/c5mt00005j
896 Boiteau, R.M., Till, C.P., Coale, T.H., Fitzsimmons, J.N., Bruland, K.W., Repeta, D.J., 2019.
897 Patterns of iron and siderophore distributions across the California Current System. Limnol.
898 Oceanogr. 64, 376–389. https://doi.org/10.1002/lno.11046
899 Buck, K.N., Sedwick, P.N., Sohst, B., Carlson, C.A., 2018. Organic complexation of iron in the
900 eastern tropical South Pacific: Results from US GEOTRACES Eastern Pacific Zonal
901 Transect (GEOTRACES cruise GP16). Mar. Chem. 201, 229–241.
902 https://doi.org/10.1016/j.marchem.2017.11.007
903 Buck, K.N., Sohst, B., Sedwick, P.N., 2015. The organic complexation of dissolved iron along
904 the U.S. GEOTRACES (GA03) North Atlantic Section. Deep. Res. Part II Top. Stud.
905 Oceanogr. 116, 152–165. https://doi.org/10.1016/j.dsr2.2014.11.016
906 Bundy, R.M., Biller, D. V., Buck, K.N., Bruland, K.W., Barbeau, K.A., 2014. Distinct pools of
907 dissolved iron-binding ligands in the surface and benthic boundary layer of the California
908 current. Limnol. Oceanogr. 59, 769–787. https://doi.org/10.4319/lo.2014.59.3.0769
909 Bundy, R.M., Boiteau, R.M., McLean, C., Turk-Kubo, K.A., McIlvin, M.R., Saito, M.A., Van
910 Mooy, B.A.S., Repeta, D.J., 2018. Distinct siderophores contribute to iron cycling in the
911 mesopelagic at station ALOHA. Front. Mar. Sci. 5, 1–15.
912 https://doi.org/10.3389/fmars.2018.00061
913 Caprara, S., Buck, K.N., Gerringa, L.J.A., Rijkenberg, M.J.A., Monticelli, D., 2016. A

914 compilation of iron speciation data for open oceanic waters. Front. Mar. Sci. 3, 1–7.
915 https://doi.org/10.3389/fmars.2016.00221
916 Croot, P.L., Heller, M.I., Wuttig, K., 2019. Redox Processes Impacting the Flux of Iron(II) from
917 Shelf Sediments to the OMZ along the Peruvian Shelf. ACS Earth Sp. Chem. 3, 537–549.
918 https://doi.org/10.1021/acsearthspacechem.8b00203
919 Crosby, H.A., Roden, E.E., Johnson, C.M., Beard, B.L., 2007. The mechanisms of iron isotope
920 fractionation produced during dissimilatory Fe(III) reduction by Shewanella putrefaciens
921 and Geobacter sulfurreducens. Geobiology 5, 169–189. https://doi.org/10.1111/j.1472-
922 4669.2007.00103.x
923 Cutter, G., Casciotti, K., Croot, P., Geibert, W., Heimbürger, L.-E., Lohan, M., Planquette, H.,
924 van de Flierdt, T., 2017. Sampling and Sample-handling Protocols for GEOTRACES
925 Cruises. Version 3, August 2017. 139pp. & Appendices.
926 https://doi.org/http://dx.doi.org/10.25607/OBP-2
927 Elrod, V.A., Berelson, W.M., Coale, K.H., Johnson, K.S., 2004. The flux of iron from
928 continental shelf sediments: A missing source for global budgets. Geophys. Res. Lett. 31,
929 2–5. https://doi.org/10.1029/2004GL020216
930 Emerson, D., Fleming, E.J., McBeth, J.M., 2010. Iron-oxidizing bacteria: An environmental and
931 genomic perspective. Annu. Rev. Microbiol. 64, 561–583.
932 https://doi.org/10.1146/annurev.micro.112408.134208
933 Fiedler, P.C., Talley, L.D., 2006. Hydrography of the eastern tropical Pacific: A review. Prog.
934 Oceanogr. 69, 143–180. https://doi.org/10.1016/j.pocean.2006.03.008
935 Gerringa, L.J.A., Rijkenberg, M.J.A., Schoemann, V., Laan, P., de Baar, H.J.W., 2015. Organic
936 complexation of iron in the West Atlantic Ocean. Mar. Chem. 177, 434–446.
937 https://doi.org/10.1016/j.marchem.2015.04.007
938 Glass, J.B., Kretz, C.B., Ganesh, S., Ranjan, P., Seston, S.L., Buck, K.N., Landing, W.M.,
939 Morton, P.L., Moffett, J.W., Giovannoni, S.J., Vergin, K.L., Stewart, F.J., 2015. Meta-omic
940 signatures of microbial metal and nitrogen cycling in marine oxygen minimum zones. Front.
941 Microbiol. 6, 1–13. https://doi.org/10.3389/fmicb.2015.00998
942 Gledhill, M., Buck, K.N., 2012. The organic complexation of iron in the marine environment: A
943 review. Front. Microbiol. 3, 1–17. https://doi.org/10.3389/fmicb.2012.00069
944 Granger, J., Price, N.M., 1999. The importance of siderophores in iron nutrition of heterotrophic
945 marine bacteria. Limnol. Oceanogr. 44, 541–555. https://doi.org/10.4319/lo.1999.44.3.0541
946 Guerinot, M. Lou, 1994. Microbial Iron Transport. Annu. Rev. Microbiol. 48, 743–772.
947 Heller, M.I., Lam, P.J., Moffett, J.W., Till, C.P., Lee, J.M., Toner, B.M., Marcus, M.A., 2017.
948 Accumulation of Fe oxyhydroxides in the Peruvian oxygen deficient zone implies non-
949 oxygen dependent Fe oxidation. Geochim. Cosmochim. Acta 211, 174–193.
950 https://doi.org/10.1016/j.gca.2017.05.019
951 Hopkinson, B.M., Barbeau, K.A., 2007. Organic and redox speciation of iron in the eastern
952 tropical North Pacific suboxic zone. Mar. Chem. 106, 2–17.
953 https://doi.org/10.1016/j.marchem.2006.02.008
954 Horak, R.E.A., Ruef, W., Ward, B.B., Devol, A.H., 2016. Expansion of denitrification and
955 anoxia in the eastern tropical North Pacific from 1972 to 2012. Geophys. Res. Lett. 43,
956 5252–5260. https://doi.org/10.1002/2016GL068871
957 Hunter, K.A., Boyd, P.W., 2007. Iron-binding ligands and their role in the ocean
958 biogeochemistry of iron. Environ. Chem. 4, 221–232. https://doi.org/10.1071/EN07012
959 Hutchins, D.A., Hare, C.E., Weaver, R.S., Zhang, Y., Firme, G.F., DiTullio, G.R., Alm, M.B.,

Riseman, S.F., Maucher, J.M., Geesey, M.E., Trick, C.G., Smith, G.J., Rue, E.L., Conn, J., Bruland, K.W., 2002. Phytoplankton iron limitation in the Humboldt Current and Peru Upwelling. Limnol. Oceanogr. 47, 997–1011. https://doi.org/10.4319/lo.2002.47.4.0997

Johnson, K., Elrod, V., Fitzwater, S., Plant, J., Landing, M., Edward, B., Bergquist, B., Bruland, K., Aguilar-Islas, A., Buck, K., Lohan, M., Smith, G.J., Sohst, B., Coale, K., Gordon, M., Tanner, S., Measures, C., Moffett, J., Barbeau, K., King, A., Bowie, A., Chase, Z., Cullen, J., Laan, P., Landing, W., Mendez, J., Milne, A., Obata, H., Doi, T., Ossiander, L., Sarthou, G., Sedwick, P., Van den Berg, S., Laglera-Baquer, L., Wu, J., Cai, Y., 2007. Developing standards for dissolved iron in seawater. Eos (Washington. DC). 88, 131–132.

Johnson, K.S., Chavez, F.P., Friederich, G.E., 1999. Continental-shelf sediment as a primary source of iron for coastal phytoplankton. Nature 398, 697–700. https://doi.org/10.1038/19511

Johnson, K.S., Gordon, R.M., Coale, K.H., 1997. What controls dissolved iron in the world ocean? Mar. Chem. 57, 137–161.

King, D.W., Lounsbury, H.A., Millero, F.J., 1995. Rates and Mechanism of Fe(II) Oxidation at Nanomolar Total Iron Concentrations. Environ. Sci. Technol. 29, 818–824. https://doi.org/10.1021/es00003a033

Klar, J.K., Schlosser, C., Milton, J.A., Woodward, E.M.S., Lacan, F., Parkinson, I.J., Achterberg, E.P., James, R.H., 2018. Sources of dissolved iron to oxygen minimum zone waters on the Senegalese continental margin in the tropical North Atlantic Ocean: Insights from iron isotopes. Geochim. Cosmochim. Acta 236, 60–78. https://doi.org/10.1016/j.gca.2018.02.031

Kondo, Y., Moffett, J.W., 2015. Iron redox cycling and subsurface offshore transport in the eastern tropical South Pacific oxygen minimum zone. Mar. Chem. 168, 95–103. https://doi.org/http://dx.doi.org/10.1016/j.marchem.2014.11.007

Kondo, Y., Moffett, J.W., 2013. Dissolved Fe(II) in the Arabian Sea oxygen minimum zone and western tropical Indian Ocean during the inter-monsoon period. Deep. Res. Part I Oceanogr. Res. Pap. 73, 73–83. https://doi.org/10.1016/j.dsr.2012.11.014

Kraemer, S.M., 2004. Iron oxide dissolution and solubility in the presence of siderophores. Aquat. Sci. 66, 3–18. https://doi.org/10.1007/s00027-003-0690-5

Kramer, J., Özkaya, Ö., Kümmerli, R., 2019. Bacterial siderophores in community and host interactions. Nat. Rev. Microbiol. 18, 152–163. https://doi.org/10.1038/s41579-019-0284-4

Laglera, L.M., Filella, M., 2015. The relevance of ligand exchange kinetics in the measurement of iron speciation by CLE-AdCSV in seawater. Mar. Chem. 173, 100–113. https://doi.org/10.1016/j.marchem.2014.09.005

Lam, P.J., Bishop, J.K.B., 2008. The continental margin is a key source of iron to the HNLC North Pacific Ocean. Geophys. Res. Lett. 35, 1–5. https://doi.org/10.1029/2008GL033294

Lam, P.J., Bishop, J.K.B., Henning, C.C., Marcus, M.A., Waychunas, G.A., Fung, I.Y., 2006. Wintertime phytoplankton bloom in the subarctic Pacific supported by continental margin iron. Global Biogeochem. Cycles 20, 1–12. https://doi.org/10.1029/2005GB002557

Lee, J.M., Boyle, E.A., Echegoyen-Sanz, Y., Fitzsimmons, J.N., Zhang, R., Kayser, R.A., 2011. Analysis of trace metals (Cu, Cd, Pb, and Fe) in seawater using single batch nitrilotriacetate resin extraction and isotope dilution inductively coupled plasma mass spectrometry. Anal. Chim. Acta 686, 93–101. https://doi.org/10.1016/j.aca.2010.11.052

Liu, X., Millero, F.J., 2002. The solubility of iron in seawater. Mar. Chem. 77, 43–54. https://doi.org/10.1016/S0304-4203(01)00074-3

1006 Lohan, M.C., Bruland, K.W., 2008. Elevated Fe(II) and dissolved Fe in hypoxic shelf waters off
1007 Oregon and Washington: An enhanced source of iron to coastal upwelling regimes.
1008 Environ. Sci. Technol. 42, 6462–6468. https://doi.org/10.1021/es800144j
1009 Lohan, M.C., Crawford, D.W., Purdie, D.A., Statham, P.J., 2005. Iron and zinc enrichments in
1010 the northeastern subarctic Pacific: Ligand production and zinc availability in response to
1011 phytoplankton growth. Limnol. Oceanogr. 50, 1427–1437.
1012 https://doi.org/10.4319/lo.2005.50.5.1427
1013 Margolskee, A., Frenzel, H., Emerson, S., Deutsch, C., 2019. Ventilation Pathways for the North
1014 Pacific Oxygen Deficient Zone. Global Biogeochem. Cycles 33, 875–890.
1015 https://doi.org/10.1029/2018GB006149
1016 Maßmig, M., Lüdke, J., Krahmann, G., Engel, A., 2020. Bacterial degradation activity in the
1017 eastern tropical South Pacific oxygen minimum zone. Biogeosciences 17, 215–230.
1018 https://doi.org/10.5194/bg-17-215-2020
1019 Mawji, E., Gledhill, M., Milton, J.A., Tarran, G.A., Ussher, S., Thompson, A., Wolff, G.A.,
1020 Worsfold, P.J., Achterberg, E.P., 2008. Hydroxamate siderophores: Occurrence and
1021 importance in the Atlantic Ocean. Environ. Sci. Technol. 42, 8675–8680.
1022 https://doi.org/10.1021/es801884r
1023 Mawji, E., Gledhill, M., Milton, J.A., Zubkov, M. V., Thompson, A., Wolff, G.A., Achterberg,
1024 E.P., 2011. Production of siderophore type chelates in Atlantic Ocean waters enriched with
1025 different carbon and nitrogen sources. Mar. Chem. 124, 90–99.
1026 https://doi.org/10.1016/j.marchem.2010.12.005
1027 McCormack, P., Worsfold, P.J., Gledhill, M., 2003. Separation and detection of siderophores
1028 produced by marine bacterioplankton using high-performance liquid chromatography with
1029 electrospray ionization mass spectrometry. Anal. Chem. 75, 2647–2652.
1030 https://doi.org/10.1021/ac0340105
1031 Millero, F.J., Sotolongo, S., Izaguirre, M., 1987. Oxidation kinetics of Fe (II) in sea water.
1032 Geochim. Cosmochim. Acta 51, 793–801.
1033 Millero, F.J., Yao, W., Aicher, J., 1995. The speciation of Fe(II) and Fe(III) in natural waters.
1034 Mar. Chem. 50, 21–39. https://doi.org/10.1016/0304-4203(95)00024-L
1035 Moffett, J.W., Goepfert, T.J., Naqvi, S.W.A., 2007. Reduced iron associated with secondary
1036 nitrite maxima in the Arabian Sea. Deep. Res. Part I Oceanogr. Res. Pap. 54, 1341–1349.
1037 https://doi.org/10.1016/j.dsr.2007.04.004
1038 Moore, C.M., Mills, M.M., Arrigo, K.R., Berman-Frank, I., Bopp, L., Boyd, P.W., Galbraith,
1039 E.D., Geider, R.J., Guieu, C., Jaccard, S.L., Jickells, T.D., La Roche, J., Lenton, T.M.,
1040 Mahowald, N.M., Marañón, E., Marinov, I., Moore, J.K., Nakatsuka, T., Oschlies, A., Saito,
1041 M.A., Thingstad, T.F., Tsuda, A., Ulloa, O., 2013. Processes and patterns of oceanic
1042 nutrient limitation. Nat. Geosci. 6, 701–710. https://doi.org/10.1038/ngeo1765
1043 Morel, F.M.M., Price, N.M., 2003. The biogeochemical cycles of trace metals in the oceans.
1044 Science (80-.). 300, 944–947. https://doi.org/10.1126/science.1083545
1045 Omanović, D., Garnier, C., Pižeta, I., 2015. ProMCC: An all-in-one tool for trace metal
1046 complexation studies. Mar. Chem. 173, 25–39.
1047 https://doi.org/10.1016/j.marchem.2014.10.011
1048 Ottley, C.J., Davison, W., Edmunds, W.M., 1997. Chemical catalysis of nitrate reduction by
1049 iron(II). Geochim. Cosmochim. Acta 61, 1819–1828. https://doi.org/10.1016/S0016-
1050 7037(97)00058-6
1051 Revsbech, N.P., Larsen, L.H., Gundersen, J., Dalsgaard, T., Ulloa, O., Thamdrup, B., 2009.

Determination of ultra-low oxygen concentrations in oxygen minimum zones by the STOX sensor. Limnol. Oceanogr. Methods 7, 371–381. https://doi.org/10.4319/lom.2009.7.371
Revsbech, N.P., Thamdrup, B., Dalsgaard, T., Canfield, D.E., 2011. Construction of STOX oxygen sensors and their application for determination of O2 concentrations in oxygen minimum zones. Methods Enzymol. 486, 325–341. https://doi.org/10.1016/B978-0-12-381294-0.00014-6
Rose, A.L., Waite, T.D., 2003. Predicting iron speciation in coastal waters from the kinetics of sunlight-mediated iron redox cycling. Aquat. Sci. 65, 375–383. https://doi.org/10.1007/s00027-003-0676-3
Rue, E.L., Bruland, K.W., 1995. Complexation of iron(III) by natural organic ligands in the Central North Pacific as determined by a new competitive ligand equilibration/adsorptive cathodic stripping voltammetric method. Mar. Chem. 50, 117–138. https://doi.org/10.1016/0304-4203(95)00031-L
Saito, M.A., Mcilvin, M.R., Moran, D.M., Santoro, A.E., Dupont, C.L., Rafter, P.A., Saunders, J.K., Kaul, D., Lamborg, C.H., Westley, M., Valois, F., Waterbury, J.B., 2020. Abundant nitrite-oxidizing metalloenzymes in the mesopelagic zone of the tropical Pacific Ocean. Nat. Geosci. 13. https://doi.org/10.1038/s41561-020-0565-6
Sandy, M., Butler, A., 2009. Microbial iron acquisition: Marine and terrestrial siderophores. Chem. Rev. 109, 4580–4595. https://doi.org/10.1021/cr9002787
Scholz, F., Löscher, C.R., Fiskal, A., Sommer, S., Hensen, C., Lomnitz, U., Wuttig, K., Göttlicher, J., Kossel, E., Steininger, R., Canfield, D.E., 2016. Nitrate-dependent iron oxidation limits iron transport in anoxic ocean regions. Earth Planet. Sci. Lett. 454, 272–281. https://doi.org/10.1016/j.epsl.2016.09.025
Tagliabue, A., Aumont, O., Bopp, L., 2014. The Impact of Different External Sources of Iron on the Global Carbon Cycle. Geophys. Res. Lett. 318, 920–926. https://doi.org/10.1002/2013GL059059.Received
Tagliabue, A., Aumont, O., DeAth, R., Dunne, J.P., Dutkiewicz, S., Galbraith, E., Misumi, K., Moore, J.K., Ridgwell, A., Sherman, E., Stock, C., Vichi, M., Völker, C., Yool, A., 2016. How well do global ocean biogeochemistry models simulate dissolved iron distributions. Global Biogeochem. Cycles 30, 149–174. https://doi.org/10.1002/2015GB005289.Received
Tagliabue, A., Bowie, A.R., Boyd, P.W., Buck, K.N., Johnson, K.S., Saito, M.A., 2017. The integral role of iron in ocean biogeochemistry. Nature 543, 51–59. https://doi.org/10.1038/nature21058
Thamdrup, B., 2000. Bacterial manganese and iron reduction in aquatic sediments, in: Advances in Microbial Ecology. pp. 41–84.
Tiano, L., Garcia-Robledo, E., Dalsgaard, T., Devol, A.H., Ward, B.B., Ulloa, O., Canfield, D.E., Peter Revsbech, N., 2014. Oxygen distribution and aerobic respiration in the north and south eastern tropical Pacific oxygen minimum zones. Deep. Res. Part I Oceanogr. Res. Pap. 94, 173–183. https://doi.org/10.1016/j.dsr.2014.10.001
Tortell, P.D., Maldonado, M.T., Price, N.M., 1996. The role of heterotrophic bacteria in iron-limited ocean ecosystems. Nature 383, 330–332. https://doi.org/10.1038/383330a0
Turner, D.R., Whitfield, M., Dickson, A.G., 1981. The equilibrium speciation of dissolved components in freshwater and sea water at 25°C and 1 atm pressure. Geochim. Cosmochim. Acta 45, 855–881. https://doi.org/10.1016/0016-7037(81)90115-0
United Nations Educational Scientific and Cultural Organization, 1994. Protocols for the Joint Global Ocean Flux Study (JGOFS) Core Measurements. New York.

1098 Van de Vossenberg, J., Woebken, D., Maalcke, W.J., Wessels, H.J.C.T., Dutilh, B.E., Kartal, B.,
1099 Janssen-Megens, E.M., Roeselers, G., Yan, J., Speth, D., Gloerich, J., Geerts, W., Van der
1100 Biezen, E., Pluk, W., Francoijs, K.J., Russ, L., Lam, P., Malfatti, S.A., Tringe, S.G.,
1101 Haaijer, S.C.M., Op den Camp, H.J.M., Stunnenberg, H.G., Amann, R., Kuypers, M.M.M.,
1102 Jetten, M.S.M., 2013. The metagenome of the marine anammox bacterium "Candidatus
1103 Scalindua profunda" illustrates the versatility of this globally important nitrogen cycle
1104 bacterium. Environ. Microbiol. 15, 1275–1289. https://doi.org/10.1111/j.1462-
1105 2920.2012.02774.x
1106 Vedamati, J., Goepfert, T., Moffett, J.W., 2014. Iron speciation in the eastern tropical south
1107 pacific oxygen minimum zone off peru. Limnol. Oceanogr. 59, 1945–1957.
1108 https://doi.org/10.4319/lo.2014.59.6.1945
1109 Velasquez, I., Nunn, B.L., Ibisanmi, E., Goodlett, D.R., Hunter, K.A., Sander, S.G., 2011.
1110 Detection of hydroxamate siderophores in coastal and Sub-Antarctic waters off the South
1111 Eastern Coast of New Zealand. Mar. Chem. 126, 97–107.
1112 https://doi.org/10.1016/j.marchem.2011.04.003
1113 Witter, A.E., Lewis, B.L., Luther, G.W., 2000. Iron speciation in the Arabian Sea. Deep. Res.
1114 Part II Top. Stud. Oceanogr. 47, 1517–1539. https://doi.org/10.1016/S0967-0645(99)00152-
1115 6
1116